JGR Oceans

RESEARCH ARTICLE
10.1029/2019JC015390

Special Section:
Recent Progresses in Oceanography and Air-Sea Interactions in Southeast Asian Archipelago

Key Points:
- Internal subseasonal variability accounts for about half of total subseasonal variabilities in the northern South China Sea
- In a ring region to the west of Luzon Strait, the internal subseasonal variability is low in the center but enhanced on the periphery
- Upscale energy transfer leads to a mean jet around the ring region, which transfers heat and kinetic energy along the circumference

Correspondence to:
L. Zhou,
zhoulei1588@sjtu.edu.cn

Citation:
Xie, J., Zhou, L., Murtugudde, R., Jochum, M., & Zhong, Y. (2020). Internal subseasonal variability in the South China Sea revealed by eddy-resolving numerical simulations. *Journal of Geophysical Research: Oceans*, *125*, e2019JC015390. https://doi.org/10.1029/2019JC015390

Received 19 JUN 2019
Accepted 12 MAR 2020
Accepted article online 16 MAR 2020

Internal Subseasonal Variability in the South China Sea Revealed by Eddy-Resolving Numerical Simulations

Juncheng Xie[1,2], Lei Zhou[3,4], Raghu Murtugudde[5], Markus Jochum[6], and Yisen Zhong[3]

[1]College of Oceanography, Hohai University, Nanjing, China, [2]State Key Laboratory of Satellite Ocean Environment Dynamics, Second Institute of Oceanography, Ministry of Natural Resources, Hangzhou,, China, [3]School of Oceanography, Shanghai Jiao Tong University, Shanghai, China, [4]Southern Marine Science and Engineering Guangdong Laboratory (Zhuhai), Zhuhai, China, [5]Department of Atmospheric and Oceanic Science, University of Maryland, College Park, MD, USA, [6]Niels Bohr Institute, University of Copenhagen, Copenhagen, Denmark

Abstract Oceanic subseasonal variabilities in the South China Sea (SCS) derive from both external forcing and internal variability. There have been extensive studies on a range of external forcings, which are composed of local and remote components. In this study, the internal subseasonal variabilities in SCS are examined using an eddy-resolving model. It is found that the internal subseasonal variabilities are pronounced in the northern SCS, which account for about half of total observed subseasonal variabilities. Particularly to the west of Luzon Strait, the internal subseasonal variabilities are enhanced on the periphery of a ring region. On the contrary, internal subseasonal variabilities are minimal in the center, which is mainly attributable to an upscale energy transfer. As a result, a mean jet is generated which transports heat and eddy kinetic energy along the edge of the ring region. We posit that the impact of internal subseasonal variabilities is significant for the background state in the region where the intense tropical cyclones occur over the northern SCS every year.

Plain Language Summary The internal subseasonal variabilities in a regional ocean are the variabilities caused by the internal oceanic processes. They are distinct from a direct response to external forcings. In the South China Sea (SCS), there have been extensive studies on oceanic subseasonal variabilities deriving from a range of external forcings. In this study, internal subseasonal variabilities are examined using a regional ocean model, which has a sufficient resolution to capture mesoscale eddies which have a typical spatial scale of hundreds of kilometers. The internal subseasonal variabilities are pronounced in the northern SCS, particularly to the west of Luzon Strait. The internal subseasonal variabilities are enhanced on the periphery of a ring region, while they are minimum in the center. In the ring region, energy is transferred from small scales to large scales, which is not common in the ocean. We posit that the impact of internal subseasonal variabilities is significant for the background state in the region where the intensive tropical cyclones occur over the northern SCS every year. Such process understandings are critical for establishing the sources of predictability and for advancing predictive understanding.

1. Introduction

The South China Sea (SCS) is a large marginal sea off southeastern Asia. The climate over SCS has profound impacts on the livelihood of a billion people in this region. Particularly, the northern SCS has the most intense tropical cyclone (TC) activities in the world (Figure 1), which cause over a thousand casualties every year in countries on the rim of SCS. The background state and variabilities in SCS are subject to both external forcing and internal variability. Each branch at various timescales deserves a dedicated examination for a comprehensive understanding of the regional ocean-atmosphere interactions over the SCS in a multiscale framework. In this study, we focus on internal subseasonal variabilities, which have a typical period of 30–60 days.

The external forcing of SCS derives from the variabilities in both the atmosphere and remote oceans at various spatiotemporal scales. SCS has a semienclosed shape with a large number of straits. It has water exchanges with the western Pacific, the Kuroshio, and the eastern China Sea through the Luzon Strait and the Taiwan Strait (Centurioni et al., 2004; Hu et al., 2000; Tian et al., 2006; Yuan et al., 2006; Xu & Oey, 2015). Although the Karimata Strait is shallow, it allows water transport from SCS to the Java Sea in the form of SCS Throughflow (Qu et al., 2006; Qu et al., 2009), which leaves a clear seasonal fingerprint

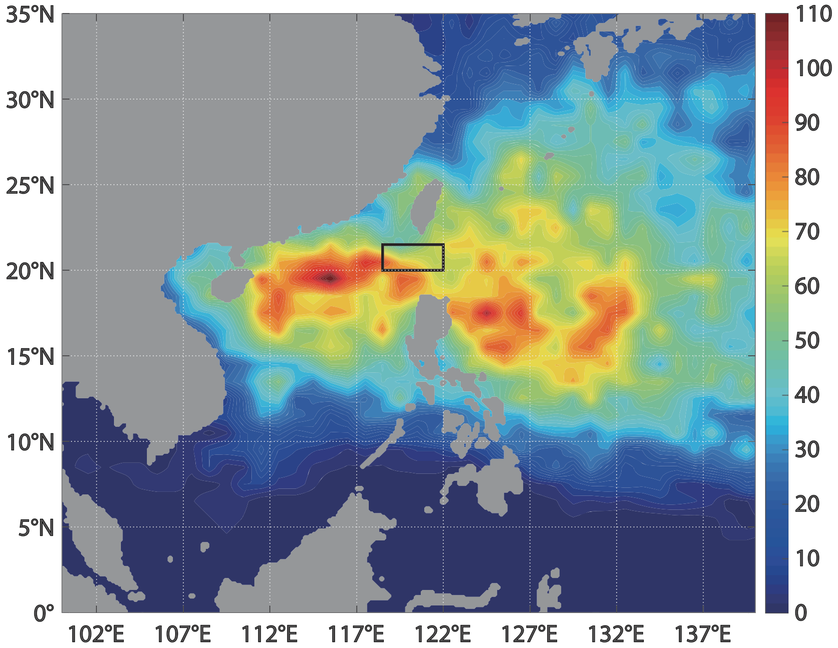

Figure 1. Accumulated number of TC occurrences over the northwestern Pacific from 1949 to 2017, based on the 6-hourly TC best track data from China Meteorological Administration (CMA; Ying et al., 2014). A TC is assumed when wind speed is larger than 17.2 m s^{-1}. The data are binned onto a regular grid with a horizontal resolution of 1° latitude × 1° longitude. The black box marks the approximate area of the ring region which is discussed below.

on the Indonesian Throughflow (Gordon et al., 2012, 2003) and is also argued to impact the Indian Ocean (Zhou et al., 2008). In the southeastern SCS, it is connected to the Sulu Sea and the Philippine Seas via complex channels (Metzger & Hurlburt, 1996; L. Yang et al., 2018). In addition, SCS is located in the East Asian monsoon region. Thus, the winds and the ocean circulation over SCS have a clear seasonal cycle (Ding et al., 2004; Lau et al., 2000; B. Wang et al., 2009, 2004, and many others). Besides, other climate processes also have distinct impacts on the SCS, such as the El Niño–South Oscillation (C. Wang et al., 2006; Zhou & Chan, 2007) at interannual timescales and the Madden–Julian Oscillation at subseasonal timescales (Sengupta et al., 2001; L. Zhang et al., 2009). At mesoscales and synoptic scales in the atmosphere, TCs have tremendous influences on SCS. They can reduce the sea surface temperature (SST) by up to 9 °C (Chiang et al., 2011; Tseng et al., 2010) and significantly modify the vertical profile of the upper ocean (I. Lin et al., 2008; Sriver & Huber, 2007; H. Zhang, Chen, et al., 2016). In addition, SCS also has significant feedbacks to TCs. Particularly, the mesoscale ocean eddies can modify the trajectory and strength of a TC rapidly, which reduces the predictability of TCs significantly (I. Lin et al., 2009; Wu et al., 2007). The strength of Typhoon Nuri was weakened by cooling of SST ahead of its path; the precooling was argued to be due to a combination of Kuroshio and stronger mixing by wind-ocean resonance (Sun & Oey, 2015; Sun et al., 2017). Based on different observations and model simulations, it is suggested that the preexistence of the cyclonic ocean eddies can enhance SST cooling and, through a negative feedback mechanism, reduce typhoon's intensity (I. Lin et al., 2005, 2008; Schade & Emanuel, 1999; Zheng et al., 2008, 2010). As shown in Figure 1, the northern SCS is a hot spot for TCs. Due to the complex topography (such as the steep continental shelf and the isolated Xisha Island), the strong ocean currents through the Luzon Strait, the intrusion of planetary waves from the Pacific Ocean (Sheu et al., 2010; H. Yang & Liu, 2003; Zheng et al., 2011), abundant ocean eddies, and instabilities occur in the northern SCS (G. Wang et al., 2003; Wu & Chiang, 2007; Xiu et al., 2010). As a result, oceanic responses and feedbacks to TCs as well as their impacts on TC forecasts are still a major scientific challenge (see Zhou et al., 2018, and related papers in that special issue). This is just a sampling of some of the SCS studies under external forcing and not intended to be comprehensive.

Ocean-TC interaction is of particular interest and scientific importance. In SCS, the TC impacts usually last for tens of days. Generally, the restoration of SST after a TC requires from a few days up to 40 days. The restoration of subsurface temperature takes a little longer (Dare & McBride, 2011; Emanuel, 2001; Guan et al., 2014; Hart, 2011; Jansen et al., 2010; Price et al., 2008). In addition, near-inertial oscillations in the upper ocean due to TCs usually decay in 15 days or longer (Chen et al., 2013; Teague et al., 2007; Tseng et al., 2010). Therefore, the TC's local and direct impacts on SCS are mainly on subseasonal timescales. Hence, a comprehensive understanding of internal subseasonal variabilities and associated mechanisms is a must for elaborating the oceanic responses to TCs in SCS. This is the motivation of this study.

To the best of our knowledge, the internal variability in SCS has not been fully explored. Oceanic internal variability is a consequence of nonlinearities and instability dynamics. The internal variability is specific to any region and can provide the basic state for its response to all external forcings. Especially, when different climate processes interact over SCS in a multiscale ocean-atmosphere coupled framework, it is a prerequisite to have a clear understanding of the internal variability of SCS before one can untangle the complex scale interactions. With this as the motivation for this study, that is, the ocean-TC interactions, we intend to focus on the internal subseasonal variabilities over SCS. The internal variabilities in the three major oceans, that is, the Pacific, the Atlantic, and the Indian Oceans, were analyzed in Jochum and Murtugudde (2004), Jochum et al. (2004), and Jochum and Murtugudde (2005). The same strategy as these previous studies is followed in this study. When diagnosing the internal variability in the Pacific Ocean in Jochum and Murtugudde (2004), only an eddy-permitting model was used. SCS was not the focus of Jochum and Murtugudde (2004), either. In this study, the focus is on SCS and an eddy-resolving model is employed to have a better understanding of its internal variability.

The rest of this paper is organized as follows. The model configurations and the data used to validate the model simulations are introduced in section 2. The internal subseasonal variabilities of SCS are diagnosed in section 3. The focus is on a ring region to the west of Luzon Strait in the northern SCS. The conclusions and discussion are presented in section 4.

2. Data and Model Configurations

The Regional Ocean Model Systems is used in this study, which is a free-surface, incompressible, hydrostatic, primitive equation ocean model with a staggered Arakawa C-grid (Shchepetkin & McWilliams, 2003, 2005). The model domain is from 90°E to 140°E and from 10°S to 30°N with a horizontal resolution of 0.1° in both longitude and latitude. The horizontal spacing of the grid is significantly smaller than the first baroclinic Rossby radius of deformation in the ocean, which is larger than 50 km for SCS (Cai et al., 2008; Chelton et al., 1998). There are 32 vertical layers in a stretched σ coordinate (Shchepetkin & McWilliams, 2005, 2011). In the upper 100 m, there are about 10 σ layers. The mixing scheme of Generic Length Scale (Umlauf & Burchard, 2003; Warner et al., 2005) is used. The open boundary conditions are obtained from the Simple Ocean Data Assimilation (SODA, version 2.2.4; Carton, Chepurin, & Cao, 2000; Carton, Chepurin, Cao, & Giese, 2000; Carton & Giese, 2008). Both inflow and outflow are nudged toward SODA. The atmospheric forcings, such as the surface wind stress, net fresh water flux (evaporation-precipitation), and surface heat fluxes, are obtained from the Climate Forecast System Reanalysis (Saha et al., 2010), which has a resolution of 0.5° in both latitude and longitude.

A control run is driven by daily climatological atmospheric forcing without any filtering. The boundary conditions are obtained from SODA reanalysis, also without any filtering. The control run is initiated from the climatological mean of SODA reanalysis and integrated for 40 years. The daily outputs for the last 10 years are used for model validation. In the control run, the simulated SST averaged for 10 years is comparable to the climatological SST obtained from the National Oceanic and Atmospheric Administration Optimum Interpolation Sea Surface Temperature (OISST) Analysis (Reynolds et al., 2002; Figure 2a). Over most of the SCS, the simulated mean SST is uniformly warmer than the climatology but by less than 0.5 °C (Figures 2a and 2b) which is likely due to the complex topography, ocean-atmosphere interactions, and the associated mixing which are not fully captured in a forced ocean simulation. Large biases of around 1 °C exist in the Maritime Continent, which however are not likely to have significant impacts on the following discussion focusing on the northern SCS. Shu et al. (2009) reported similar biases over 1 °C in the same region. The simulated mean sea surface heights (SSHs) are also comparable to observations (averaged from 1995 to 2014), which are obtained from the Archiving, Validation, and Interpretation of Satellite Oceanographic (AVISO) merged satellite data with a horizontal resolution of 0.5° in both latitude and

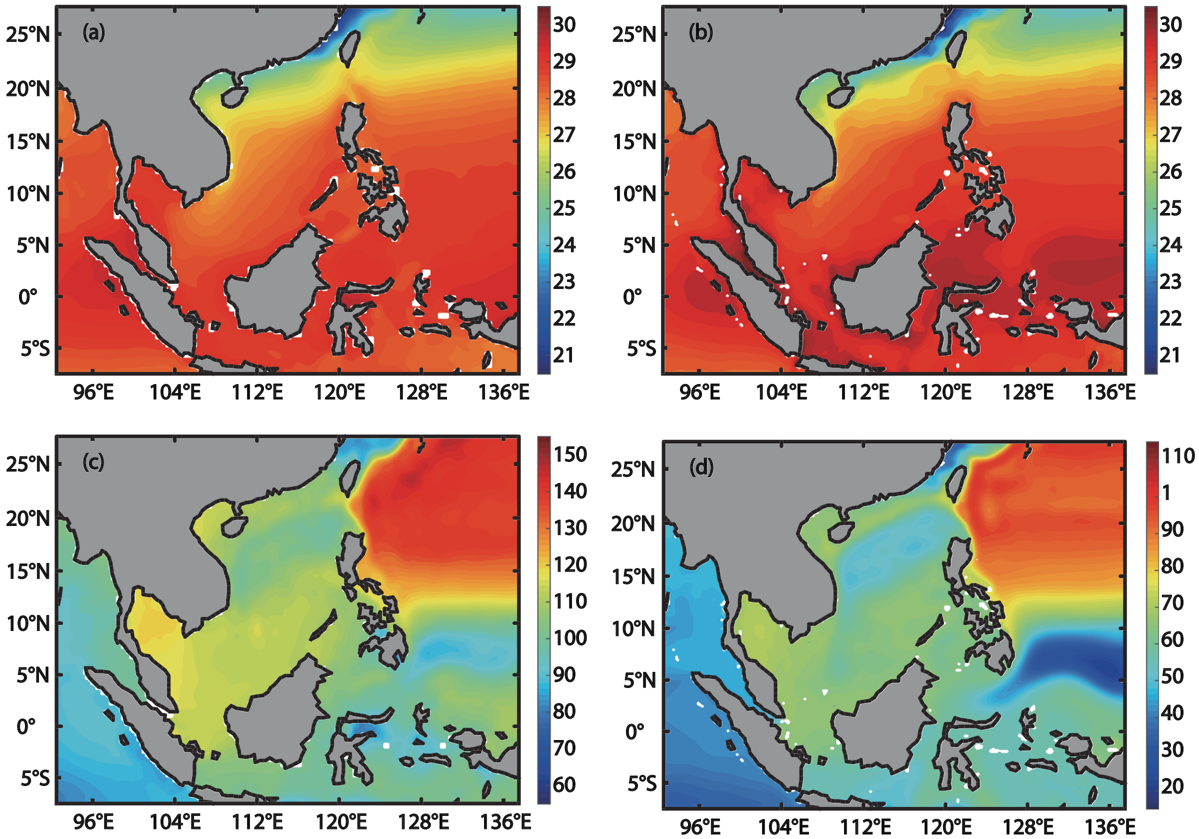

Figure 2. (a) Mean OISST averaged from 1995 to 2014 and (b) mean simulated SST in the control run for 10 years. The unit for SST is °C. (c, d) The same as (a) and (b) but for the comparisons between the mean SSH from AVISO data (averaged from 1995 to 2014) and those from the control run. The unit for SSH is cm.

longitude (Ducet et al., 2000; Figure 2c). The patterns of simulated and observed SSH are similar, but the simulated SSH have a systematic negative bias. Negative SSH biases around −60 cm occur in the western Pacific (between 6°N and 12°N) and in the Indian Ocean (Figures 2c and 2d). Around the Luzon Strait, which is the focus in the following analysis, and along the Kuroshio, SSH biases are generally no larger than −30 cm (Figures 2c and 2d). Along the Kuroshio, the biases are within −30 to 10 cm. The surface ocean currents are comparable with geostrophic currents estimated using AVISO data. Particularly, along Kuroshio and around Luzon Strait, the differences in mean current speeds are no larger than 0.2 m s^{-1} (not shown).

The temperature profiles along 20°N are compared between the control run and World Ocean Atlas 2013 (WOA13, version 2, Locarnini et al., 2013) in Figure 3. The isothermal slope across the Luzon Strait (from 120°E to 122°E) due to the temperature contrasts between the western Pacific and SCS is captured in the control run. The temperature stratification of WOA13 and control run is similar. Where for depths shallower than 50 m, the temperature reaches 27–28 °C, and the agreements between control and WOA13 are good in the west and east of Luzon Strait. In deeper regions, the temperature of the control run is cooler than that of WOA13 by about 2 °C to the west of Luzon Strait, and by about 0.5 °C colder than WOA13 to the east of Luzon Strait. Using the Princeton Ocean Model, Sun et al. (2015, 2017) reported a model bias of 1 °C in temperature simulations.

The simulated subseasonal variabilities are compared with observations in Figure 4. The subseasonal SST anomalies are pronounced in the northern SCS and off Vietnam, where their STDs are larger than 0.5 °C. In the southern SCS, the subseasonal SSTs are weaker with STDs smaller than 0.45 °C (Figure 4a). In the control run, the spatial distribution of subseasonal SSTs is similar to observations (Figure 4b); that is, they are large in the northern SCS and off Vietnam but small in other regions. However, the simulated amplitudes are smaller than observations. In the northern SCS, the STDs of simulated subseasonal SST anomalies are

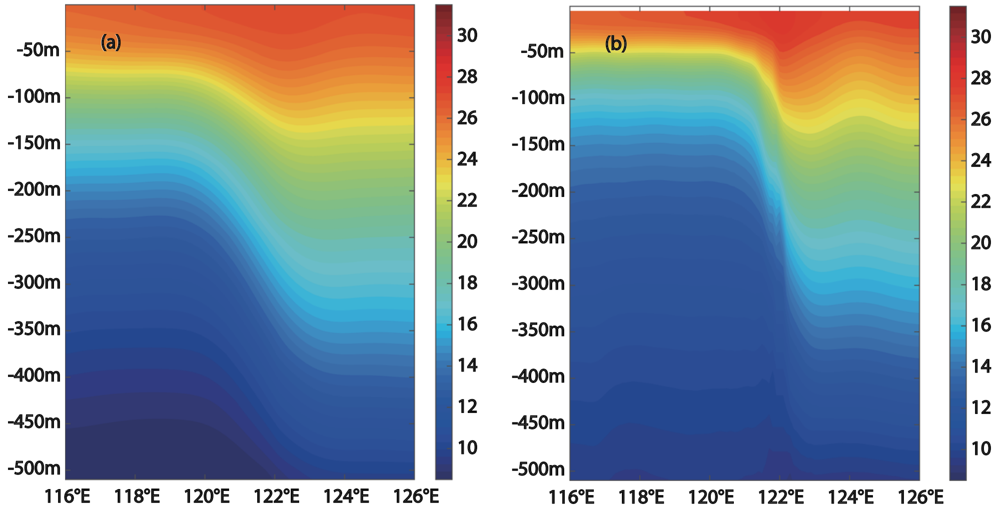

Figure 3. Vertical temperature profiles from WOA13 (a) and from the control run (b) along 20°N. The unit is °C.

about 60% of those in observations (Figure 4c). In the southern SCS, the variance of subseasonal SST anomalies in the control run reduces to 40% of the observations. However, near the Luzon Strait, which is the key region for the following analyses, the ratio between simulated and observed STDs of subseasonal SST anomalies is close to 1 (reddish colors in Figure 4c), which indicate that the amplitude of simulated subseasonal variabilities is comparable with observations. The same comparisons are conducted for subseasonal SSH anomalies, and the results are shown in Figures 4d–4f. The STDs of subseasonal SSH anomalies from AVISO are larger than 4 cm in the northern SCS and off Vietnam, but they are smaller than 3 cm in the southern SCS (Figure 4d). This spatial pattern is captured by the control run (Figure 4e). There are pronounced subseasonal SSH anomalies along the South China coast and in the Beibu Gulf in AVISO data (Figure 4d) but not in the control run (Figure 4e). However, the tides and high-frequency atmosphere forcing can be aliased into the low-frequency variabilities. As a result, the altimeter data may not be accurate in shallow waters (Zhuang et al., 2010). Over most of the SCS, the simulated variance of subseasonal SSH is over 80% of those from altimeter data (Figure 4f). Particularly, near the Luzon Strait, the simulated subseasonal SSHs are comparable with the observations (reddish colors in Figure 4f).

In order to unveil the dynamics of internal subseasonal variabilities, which can serve as a basis for further studies on local oceanic response to TCs, an internal variability run is conducted. In the internal run, all variabilities with a frequency higher than the subseasonal timescales are removed from the atmospheric forcing and the boundary conditions, using a Butterworth low-pass filter with a cutoff period of 100 days. In addition, the mesoscale variabilities with a spatial scale smaller than the Rossby radius of deformation in the atmosphere are also removed from the atmospheric forcing, using a low-pass filter with a cutoff wavelength of 2,000 km (the first baroclinic Rossby radius of deformation in the atmosphere in most part of SCS is around 2,000 km; not shown). For the surface wind forcing, all filters are applied to surface wind stress, rather than the wind velocities. Although the width of SCS is smaller than 2,000 km, it is verified that the mean vertical temperature structures in the control run and the internal run are comparable with those in WOA13, and they are not heavily influenced by the cutoff wavelength of 2,000 km (not shown). Since all mesoscale and subseasonal variabilities in the external forcing (both the atmospheric forcing and the boundary conditions) have been removed, all simulated mesoscale and subseasonal variabilities in the ocean in the internal run can only be attributed to oceanic internal variabilities generated by nonlinear interactions. In the following analysis, all results are obtained using the outputs of the internal run and all subseasonal variabilities are obtained using a high-pass filter with a cutoff period of 100 days.

3. Results

The STDs of simulated subseasonal variabilities in the internal run are shown in Figure 5a. In nature, subseasonal variabilities are pronounced in the northern SCS and off Vietnam where their STDs are larger than

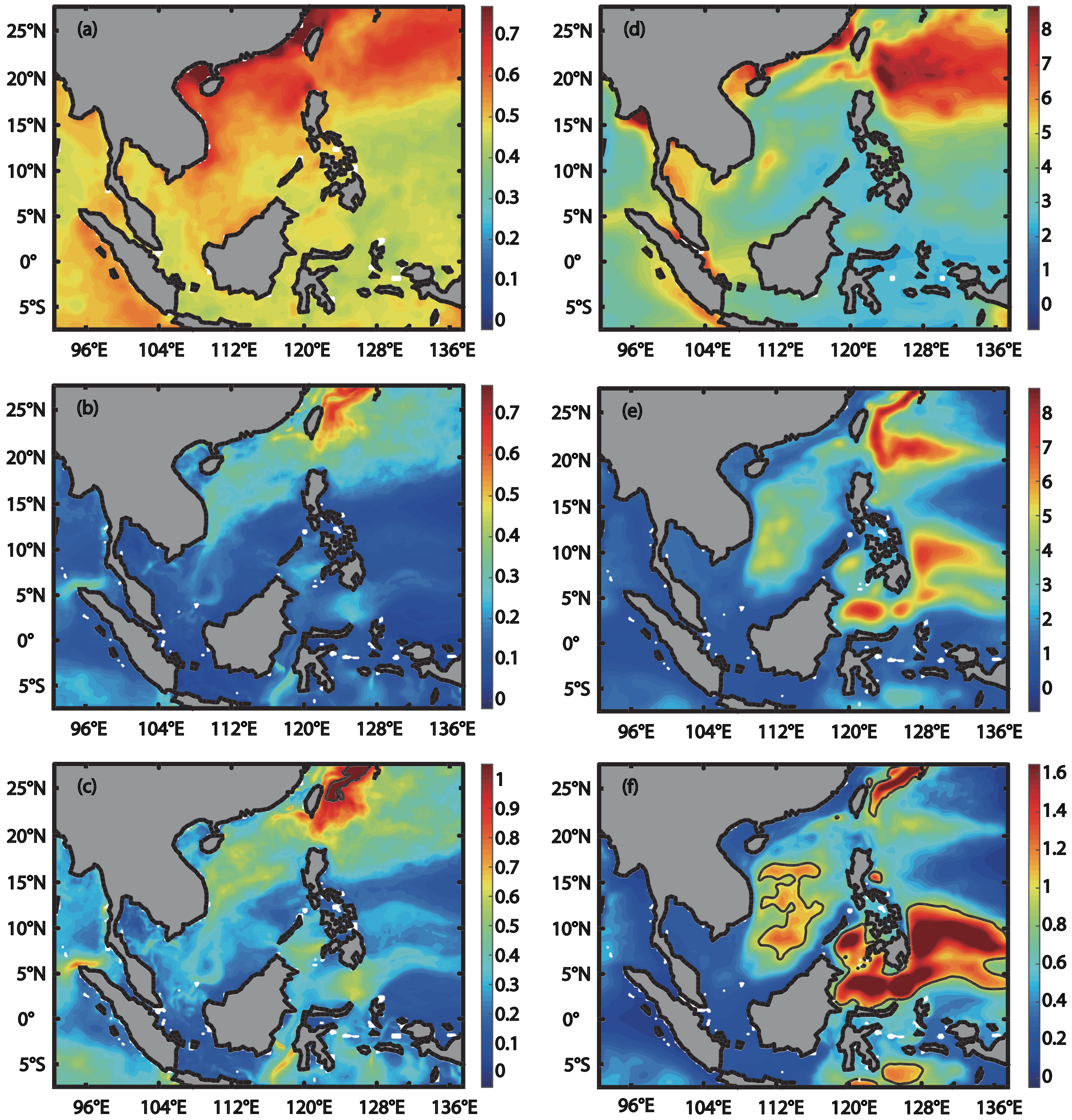

Figure 4. (a) STDs of subseasonal OISST. (b) STDs of simulated subseasonal SST in the control run for 10 years. The unit for SST is °C. (c) Ratio between the STDs of subseasonal SST from the control run and those from OISST. (d–f) The same as (a)–(c) but for the comparisons between the STDs of subseasonal SSH from the control run and those from AVISO data. The unit for SSH is cm.

0.5 °C. In contrast, in the southern SCS, the subseasonal SST anomalies are weak with STDs smaller than 0.4 °C (Figure 4a). In the northern SCS, subseasonal variabilities due to oceanic internal variability account for about half of the total subseasonal variabilities in observations (Figure 5b). Nevertheless, in the southern SCS, the internal subseasonal variabilities only account for about 20% or less of the total subseasonal variabilities. Therefore, internal subseasonal variability is generally a prominent component for the climate over the northern SCS. In addition, over most of SCS, subseasonal variabilities from internal run simulations account for over 80% of the subseasonal variabilities from control run simulations (Figure 5c).

All variables can be decomposed into a subseasonal component (denoted with a prime) and a background component which has a period longer than a season (denoted with an overbar; Jochum &

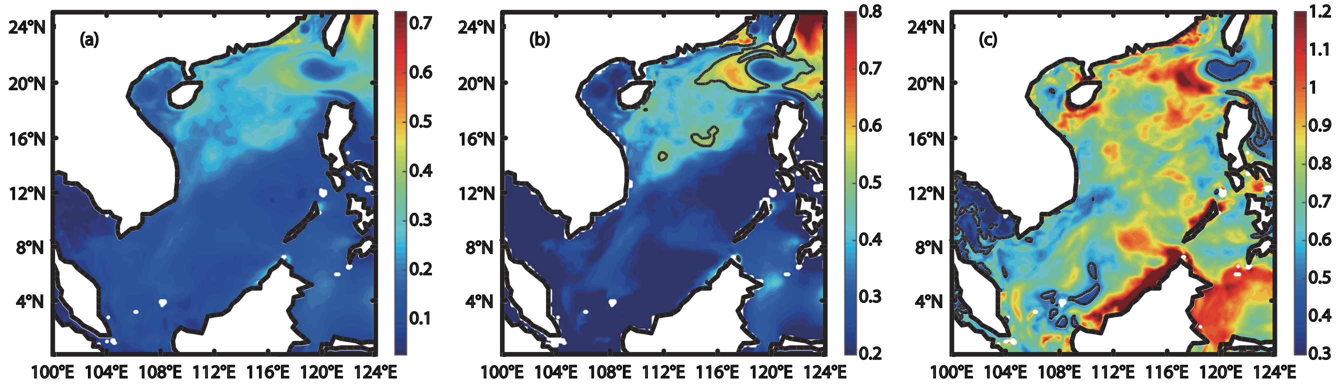

Figure 5. (a) STDs of simulated subseasonal SST from the internal run. The unit is °C. (b) Ratio between the STDs of subseasonal SST from the internal run and those from daily OISST. (c) Ratio between the STDs of subseasonal SST from the internal run and those from the control run. The black contours mark the ratio of 0.5.

Murtugudde, 2006). Then, the thermodynamic equation for the upper ocean mixed layer on the subseasonal timescale can be written as (see Appendix A for details)

$$\frac{\partial T'}{\partial t} = H'_{adv} + V'_{adv} + Ent' + \frac{Q'_{surf}}{\rho C_p \overline{h}} + R' \tag{1}$$

where T is the sea water temperature; $\cdot = \frac{1}{h}\int_{-h}^{0} \cdot \mathrm{d}z$ denotes the average within the upper mixed layer, h is the mixed layer depth (MLD); $H'_{adv} = -\overrightarrow{\overline{V}}_H \cdot \nabla_\mathrm{H} T' - \overrightarrow{V'}_H \cdot \nabla_\mathrm{H} \overline{T} - \left(\overrightarrow{V}'_H \cdot \nabla_\mathrm{H} T' - \overline{\overrightarrow{V}'_H \cdot \nabla_\mathrm{H} T'} \right)$ denotes horizonal advection at subseasonal timescale, $\overrightarrow{V}_H = u\overrightarrow{i} + v\overrightarrow{j}$ is the horizontal ocean current, $\nabla_\mathrm{H} = \frac{\partial}{\partial \mathrm{x}}\overrightarrow{i} + \frac{\partial}{\partial \mathrm{y}}\overrightarrow{j}$, $\overrightarrow{i}$ and $\overrightarrow{j}$ are unit vectors in the eastward and northward directions, respectively; $V'_{adv} = -w\frac{\partial T'}{\partial z}$ denotes vertical advection; $Ent' = \left[\frac{1}{h}\frac{\partial h}{\partial t}\left(T|_{z=-h} - T\right)\right]'$ denotes entrainment at subseasonal timescale; Q_{surf} is the net surface heat flux, ρ is water density, and $C_p = 4{,}096$ J·kg^{-1}·K^{-1} is the heat capacity at a constant pressure; R denotes the sum of eddy diffusivities (both vertical and horizontal which depend on model parameterization) and a residual term. MLD is the depth where the temperature is lower than SST by 0.5 °C (Monterey & Levitus, 1997). As argued before, since all subseasonal and mesoscale variabilities in the external forcing are removed, the subseasonal component in the internal run simulations is only attributable to the oceanic internal variability due to nonlinear interactions. Although the large-scale component in the ocean can have discernible patterns in the responses to atmospheric forcing, it will be shown later that a stochastic background component can also be generated due to the oceanic internal subseasonal variability via an upscale energy cascade.

Figure 6 shows the composites of major terms in the subseasonal heat budget for the mixed layer (equation 1). For each grid point, the days used to make the composites satisfy two criteria. One is that the simulated subseasonal SST anomaly is larger than the mean plus the STDs of the 10 year simulated subseasonal SST anomalies at the same grid point. The other is that the days have a maximum subseasonal SST anomalies within 30 consecutive days (about half of a subseasonal period). The tendency of T', which is only pronounced over the northern SCS (not shown), is mainly attributable to horizontal advection (Figure 6a). The subseasonal entrainment is another discernible term in the heat budget (Figure 6b). All other terms in equation 1 are small enough to be neglected. Particularly, the heat gain via the net surface heat flux ($\frac{Q'_{surf}}{\rho C_p \overline{h}}$) is not an important term in equation 1, since the subseasonal component in Q_{surf} is removed by design. In addition, zonal advection dominates the horizontal advection (Figures 6c and 6d). Both subseasonal SST and current anomalies propagate westward in SCS at a speed around 0.1 m s^{-1} (Figure 7), which is consistent with the phase speed of the first baroclinic Rossby wave around 20°N (Liu et al., 2001). There are also westward

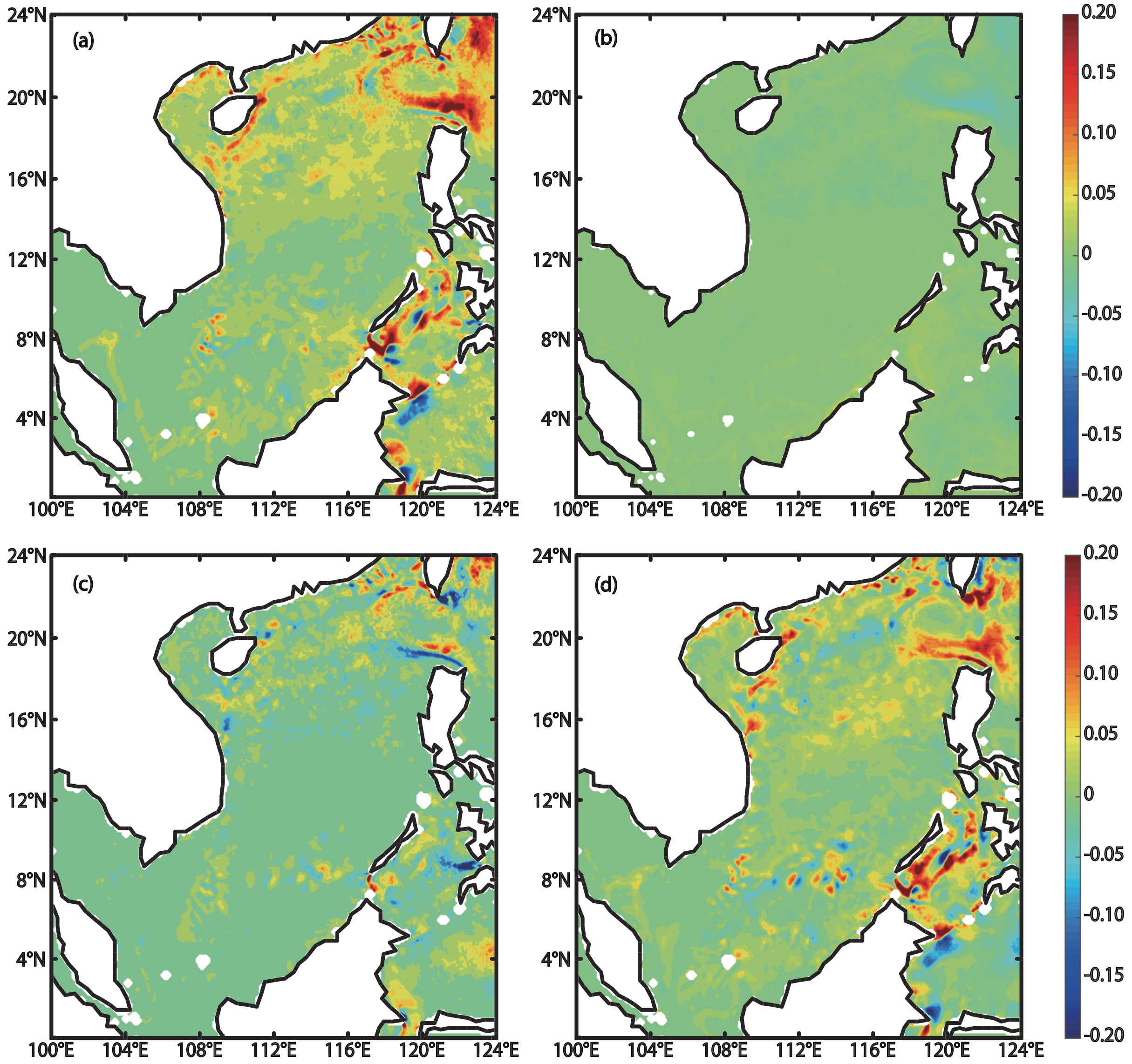

Figure 6. Composites of major terms in the mixed layer heat budget (equation 1). For each grid point, the composites are made with days satisfying two criteria which are specified in the main text. Panel (a) is for the composite H'_{adv}, (b) is for the composite Ent', (c) is for $-\bar{u}\frac{\partial T'}{\partial x}$, and (d) is for $-u'\frac{\partial \bar{T}}{\partial x}$. The unit is °C day^{-1}.

propagating Rossby waves over the western Pacific (to the east of dash-dotted lines in Figure 7; Chelton & Schlax, 1996). In SCS, some Rossby waves originate from the Pacific and enter through the Luzon Strait, while some are generated locally. Evidence can be found for both sides of the ongoing debate about whether the waves in the Pacific can effectively invade SCS (Hu et al., 2012; Qu et al., 2000; M. Zhang, Zhou, et al., 2016). In SCS, Rossby waves have been extensively studied (e.g., Hu et al., 2012; Y.-C. Lin et al., 2016; H. Yang & Liu, 2003; Xie et al., 2007). Perturbations generated by the nonlinear internal variabilities are also adjusted in the form of Rossby waves and spread over the northern SCS. Such conclusions are straightforward and in concert with the existing dynamics in SCS.

Although the subseasonal SST anomalies due to oceanic internal subseasonal variability are generally large in the northern SCS, they are distinct on the periphery of the ring region to the west of the Luzon Strait. As shown in Figures 5a and 5b, the STDs of simulated subseasonal SST anomalies can reach 0.3 °C and account for over 60% of the total observed subseasonal SST variabilities. The subseasonal SST variance is comparable with those in equatorial oceans (Schott et al., 2009; Shinoda et al., 1998; Waliser et al., 2003, 2004), which

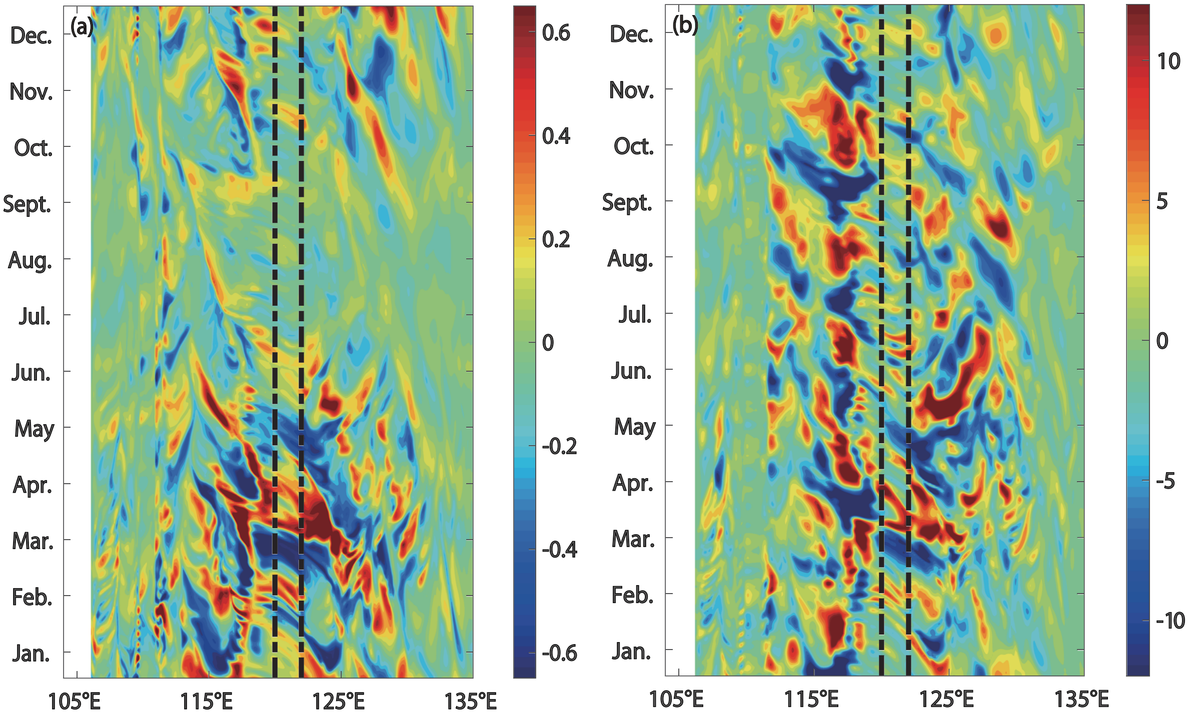

Figure 7. Hovmöller diagrams of subseasonal SST anomalies (a) and subseasonal zonal current anomalies (b) averaged between 19.5°N and 20.5°N in Year 5 from the internal run. The diagrams for other years are similar. The two dash-dot lines mark the location of Luzon Strait. The unit for SST is °C, and the unit for zonal current is cm s^{-1}.

have been demonstrated to be important for the ocean-atmosphere interaction in the tropics. In addition, mean SST in northern SCS is around 27.5 °C (Figure 2b), which is the threshold for deep convection in the atmosphere (Graham & Barnett, 1987). Therefore, the subseasonal SST variance of 0.3 °C can be critical for organizing deep convection and for the oceanic feedback to TCs. In contrast, the center of the ring region is tranquil, where the STDs of subseasonal SST variabilities are merely about 0.1 °C. Correspondingly, internal subseasonal variability has a contribution of only about 30% to the observed subseasonal variability which is much lower than the surrounding regions. Figure 8a shows the time series of subseasonal SST anomalies averaged in Box A (within 116.5–117.5°E and 19.9–21.1°N; marked in Figure 8b) on the periphery of the ring region. The days for composites are selected following the above two criteria; that is, on the selected days, the subseasonal SST anomalies are larger than their mean plus their STDs, and the subseasonal SST anomalies are at their maximum in 30 consecutive days. Such days (referred to as Day 0 hereafter) are marked with red circles in Figure 8a, and the following composite analyses are conducted with respect to these days. The composite subseasonal SST anomalies are as large as 0.4 °C on the periphery, while they are uniformly small (less than 0.1 °C) in the center. In addition, the MLD is uniformly deep (~80 m) at the center and rapidly shoals to shallower than 60 m toward the periphery (white contours in Figure 8b). The composite heat budget terms with respect to Day 0 (red cycles in Figure 8a) are shown in Figure 9a. It is obvious that the subseasonal temperature changes due to horizontal advection (red line) agree well with the tendency of $T^{'}$ (black line). The temperature changes due to horizontal advection are partly offset by the sum of mixing and residual terms (green line). All other terms are small. Since the surface heat flux is low-pass filtered, the contribution derived from $Q^{'}_{surf}$ (cyan line) is negligible. Moreover, one can see from Figure 9b that the subseasonal temperature anomaly advected by the background meridional ocean currents, that is, $-\overline{v}\frac{\partial T^{'}}{\partial y}$, dominates the total horizontal advection. In fact, it controls the tendency of T'. Box A on the periphery is to the west of the ring region. Another box, Box B (120–122°E and 19.5–20°N; Figure 8b), is selected to the south of the periphery, and the above conclusion remains robust. The subseasonal temperature anomalies advected by the

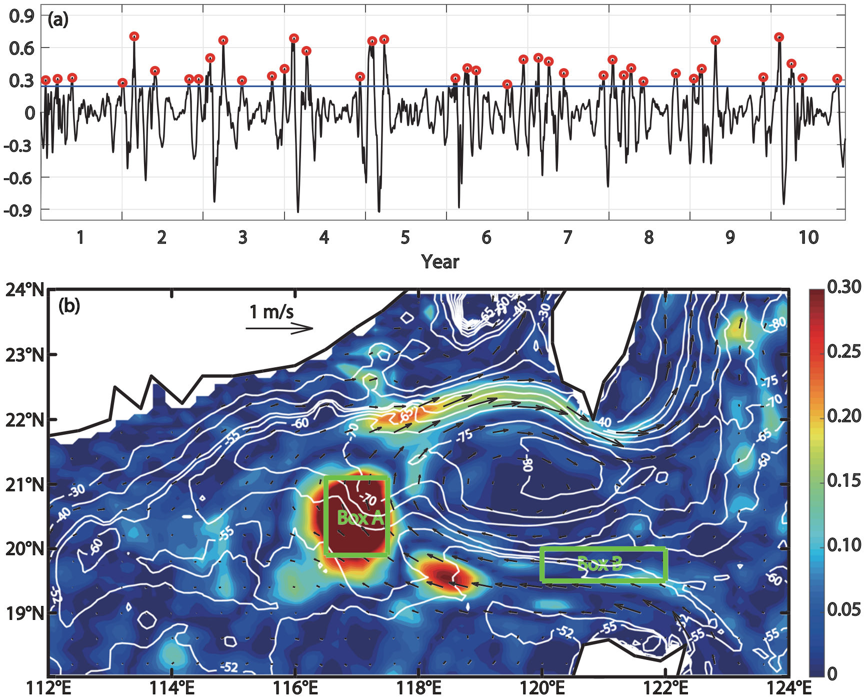

Figure 8. (a) Subseasonal SST anomalies averaged in Box A (within 116.5–117.5°E and 19.9–21.1°N) on the periphery of the ring region. The STDs of subseasonal SST anomalies are shown with the blue line. The unit is °C. Reference days (Day 0) for the following composite are marked with red circles. See main text for the detailed methods to determine reference days. (b) Composite subseasonal SST anomalies (colors, unit: °C) and composite background surface currents (black vectors with respect to Day 0 marked with red circles in (a)). White contours show mean MLD in meters.

background zonal current ($-\overline{u}\frac{\partial T'}{\partial x}$) overwhelm the heat budget (Figures 9c and 9d). Sensitivity tests are performed by using Boxes A and B with different sizes. The results of the heat budget analysis remain robust (not shown). Therefore, it can be concluded that the subseasonal SST anomalies are attributable to advection by the background circular ocean currents along the ring region. Such a pattern can be clearly seen in Figure 8b. The circular currents originate from the southern part of the Luzon Strait, which is due to the conservation of quasi-geostrophic potential vorticity modified by the bottom topography (Lu & Liu, 2013) and to local wind stress curl (Xu & Oey, 2015). Note that the ocean currents dominant in advection are in fact the low-frequency components, which are obtained with a low-pass filtering of 100 days. However, there are no corresponding components in the atmospheric forcing (not shown). In addition, the circular background currents along the ring region (Figure 8b) have a much smaller spatial scale (particularly in the radial direction) than those in the atmospheric wind, heat, or freshwater flux forcing. The radius of the ring is about 300 km, which is comparable to the spatial scale of mesoscale eddies in SCS. The radial width of the background currents is about 80 km, which is more like a jet.

In addition to the temperature anomalies in the mixed layer, the kinetic energy is also enhanced at subseasonal timescales and shows a similar pattern as that of temperature anomalies. The kinetic energy equation at subseasonal timescales can be written as (Holton & Hakim, 2013; Zhou et al., 2012)

$$\frac{\partial KE'}{\partial t} = -\overrightarrow{\overline{V}\cdot\nabla \mathrm{KE}'} + \left[KE'\cdot\overline{KE}\right] + \left[KE'\cdot PE'\right] + \mathrm{PGF} + \mathrm{EV} \tag{2}$$

where $KE' = \frac{1}{2}\left(u'^2 + v'^2 + w'^2\right)$ is the kinetic energy anomaly, $\overrightarrow{V}$ is the three-dimensional ocean current, $\nabla = \frac{\partial}{\partial \mathrm{x}}\overrightarrow{i} + \frac{\partial}{\partial y}\overrightarrow{j} + \frac{\partial}{\partial z}\overrightarrow{k}$, $-\overrightarrow{\overline{V}\cdot\nabla KE'}$ stands for the advection of KE' by the background currents, $\left[KE'\cdot\overline{KE}\right] =$

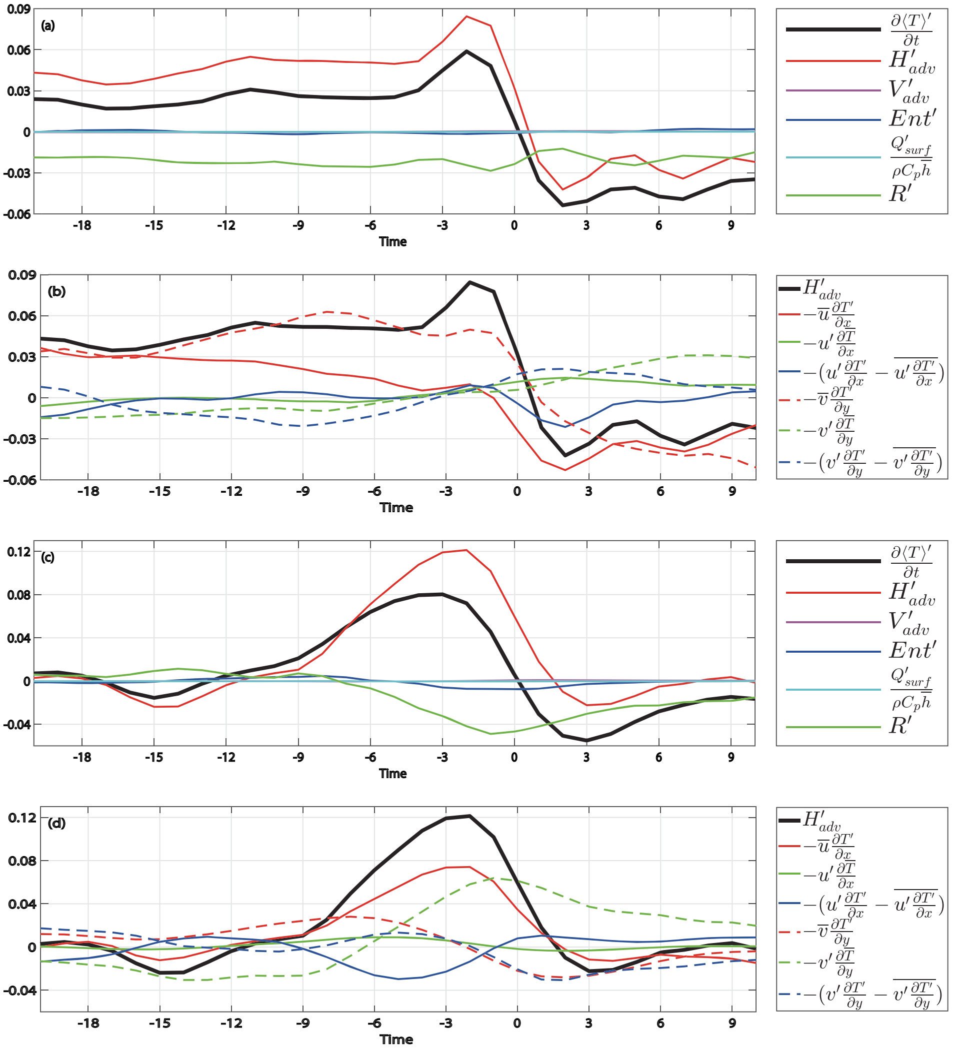

Figure 9. (a) Composite heat budget terms averaged over Box A (Figure 8b) on the western part of the periphery of the ring region with respect to Day 0 marked with red circles in Figure 8a. (b) Composite components of horizontal advection. (c, d) The same as (a) and (b) but for Box B in Figure 8b. The unit is °C day^{-1}.

$-u^{'}\left(\overrightarrow{V}^{'}\cdot\nabla\right)\overline{u}-v^{'}\left(\overrightarrow{V}^{'}\cdot\nabla\right)\overline{v}$ stands for the kinetic energy exchange between the subseasonal and the mean scales, $\left[KE^{'}\cdot PE^{'}\right]=-w^{'}g\frac{\rho^{'}}{\overline{\rho}}$ stands for the energy exchange between the kinetic and potential energies at subseasonal timescales, g is the gravitational acceleration, $\mathrm{PGF}=-\overrightarrow{V}^{'}_{H}\cdot\nabla_{H}\phi^{'}$ denotes the work done by the pressure gradient force, and EV denotes the kinetic energy changes due to the nonlinear processes whose explicit form is $-u^{'}\left(\overrightarrow{V}^{'}\cdot\nabla u^{'}-\overline{\overrightarrow{V'}\cdot\nabla u^{'}}\right)-v^{'}\left(\overrightarrow{V}^{'}\cdot\nabla v^{'}-\overline{\overrightarrow{V'}\cdot\nabla v^{'}}\right)$. See Appendix B for the detailed derivations.

The composite terms in the kinetic energy budget (equation 2) averaged within Box A (Figure 8b) are shown in Figures 10a and 10b. The subseasonal $KE^{'}$ (black line) increases before Day 0, which is coherent with the subseasonal SST anomalies. The advection of $KE^{'}$ by the background currents explains the enhancement of $KE^{'}$, which also agrees with the subseasonal temperature advection by the background currents. $\left[KE^{'}\cdot\overline{KE}\right]$ is another pronounced term in the budget. But it is always negative, which indicates that $KE^{'}$ is transferred to $\overline{KE}$ via an inverse energy cascade. All other terms, including the residual term, are small in Figure 10a. $[KE^{'}\cdot PE^{'}]$ is small because it is not calculated for the total upper ocean. Using a different eddy-resolving model, the eddy energy budget in the SCS was examined by H. Yang et al. (2013). They also reported an

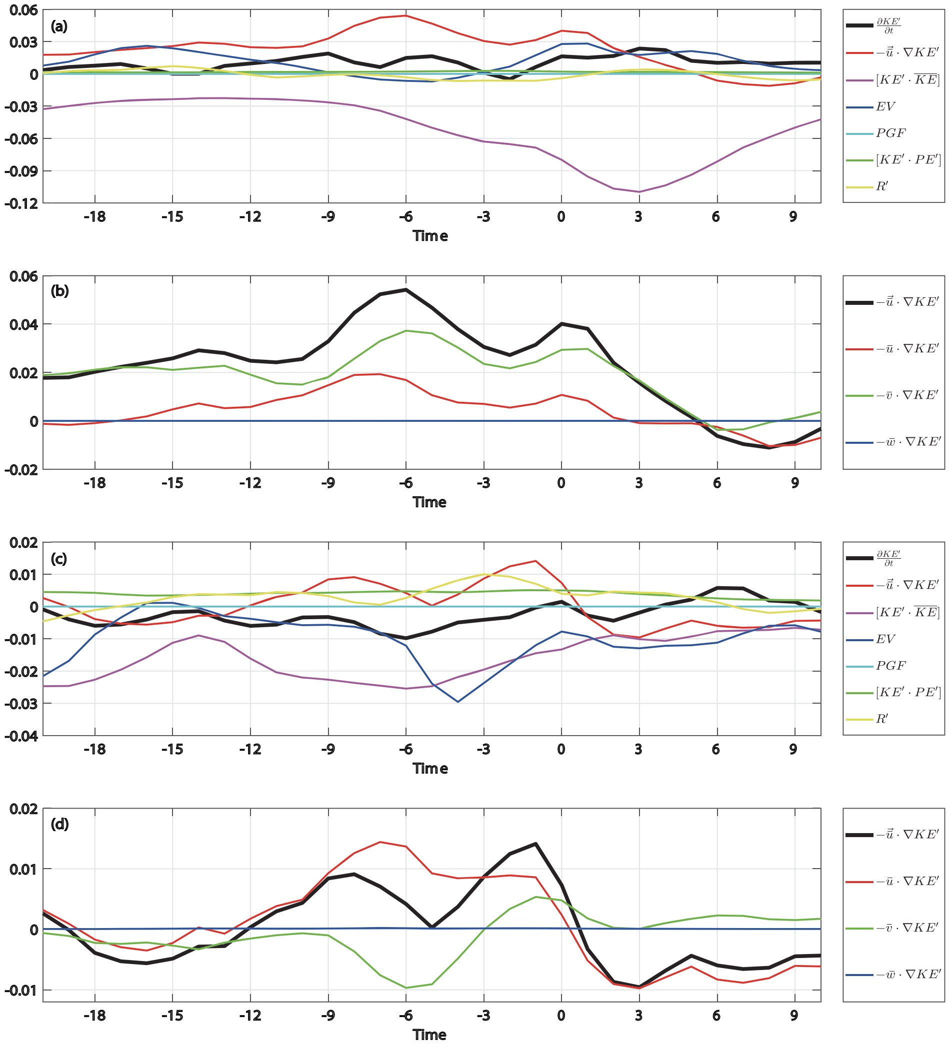

Figure 10. (a) Composite terms in kinetic energy budget for KE' (equation 2) averaged over Box A (Figure 8b) on the western part of the periphery of the ring region with respect to Day 0 marked with red circles in Figure 8a. (b) Composite components of horizontal advection terms in KE' budget. (c, d) The same as (a) and (b) but for Box B in Figure 8b. The unit is 0.1 J·day^{-1}·kg^{-1}.

upscale kinetic energy exchange between the eddy and the mean scales to the south of Luzon Strait (see their Figure 4d). The same conclusion can be drawn with the composites for Box B in Figure 8b, as shown in Figures 10c and 10d. The only difference with respect to Box A is that the advection of KE' by the background zonal currents dominates, since Box B is to the south of the ring region. Such a difference is also consistent with the contrast in temperature advection between Figures 9b and 9d. The results of the kinetic energy budget analysis are not sensitive to the selection of Boxes A and B (not shown).

Two-dimensional geostrophic turbulence enables such inverse energy cascade from small scales to large scales. Theoretically, the interface between the planetary waves and turbulence by matching the Rossby wave period and the turnover time for eddies in the direction of energy transfer is on the scale of $L_\beta \sim \left(\frac{\epsilon}{\beta^3}\right)^{1/5}$, where ϵ is the energy dissipation rate and β is the meridional gradient of Coriolis parameter (Vallis, 2006). There is no straightforward way to estimate ϵ. In this study, ϵ is estimated as the tendency of subseasonal kinetic energy, that is, $\partial KE'/\partial t$, which can be regarded as an upper limit of ϵ. In fact, L_β is proportional to $\epsilon^{1/5}$. If ϵ increases by 1 order of magnitude (10 times), L_β only increases by less than 1.6. Thus, the estimate of L_β is not very sensitive to the estimate of ϵ. The distribution of L_β in the northern SCS is shown in

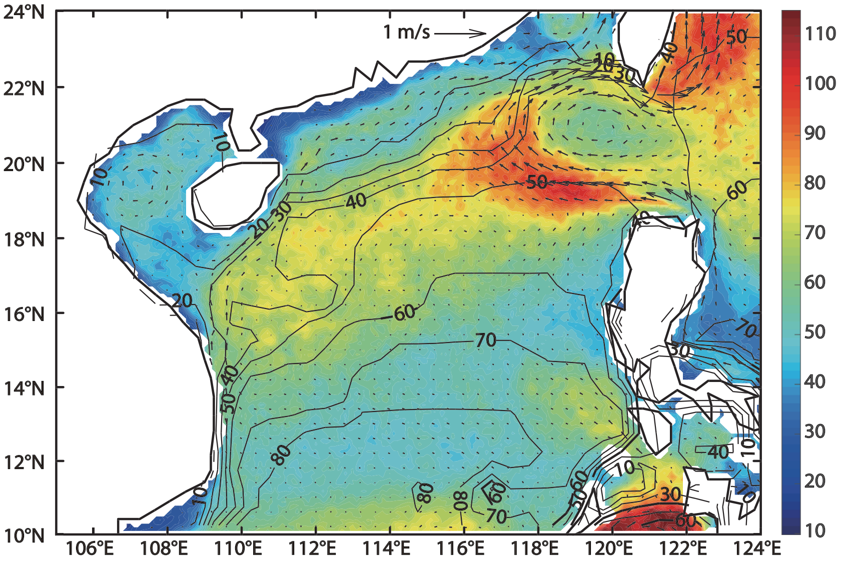

Figure 11. Distribution of L_β (colors) and the first baroclinic Rossby radius of deformation (black contours). The unit is km. Background currents are superimposed with arrows.

Figure 11 (colors), superimposed with the first baroclinic Rossby radius of deformation (L_d; black contours). In northern SCS, L_d is smaller than 60 km and decreases with latitudes. In most regions of the northern SCS, the estimated L_β is larger than 70 km. On the periphery of the ring region, L_β is around 100 km, which is larger than L_d. Therefore, Rossby waves control the energy distribution in most northern SCS, which is clearly seen in Figure 7, and the inverse energy cascade cannot occur. In contrast, at the center of the ring region, L_β is between 40 and 60 km (colors in Figure 11), which is comparable to L_d (black contours in Figure 11). It is well known that L_d is a critical length scale for instabilities. For example, in the classical Eady problem, the wavenumber for the greatest unstable wave is $k_d = \frac{1.6}{L_d}$ (Vallis, 2006; Zhou et al., 2008). Therefore, in the center of the ring region, k_d is comparable with $k_\beta = \frac{1}{L_\beta}$.

Moreover, the inverse energy cascade can be quantitatively shown by examining the spectral kinetic energy flux Π_ω (Scott & Arbic, 2007; Scott & Wang, 2005). For any given cutoff frequency ω, high-frequency (low-frequency) variabilities with a frequency higher (lower) than ω are obtained with a high-pass (low-pass) filtering. The high-frequency horizontal velocities are denoted with $\overrightarrow{u}'_\omega$, and the low-frequency horizontal velocities are denoted with $\overline{\overrightarrow{u}}_\omega$ (note that the overbar does not denote a temporal mean but a low-frequency component).

Following Scott and Wang (2005), the kinetic energy for the low-frequency kinetic energy can be written as (see details in Appendix C)

$$\frac{\partial \overline{KE}_\omega}{\partial t} = -\Pi_\omega + \mathscr{F} - \mathscr{D}, \tag{3}$$

where $\overline{KE}_\omega = \frac{1}{2}\left(\overline{\overrightarrow{u}}_\omega \cdot \overline{\overrightarrow{u}}_\omega\right)$ denotes the low-frequency kinetic energy at a given frequency ω; we can obtain the spectral kinetic energy flux $\Pi_\omega = -\overrightarrow{u}'_\omega \cdot \left[\left(\overrightarrow{u}'_\omega \cdot \nabla\right)\overline{\overrightarrow{u}}_\omega\right]$, which is also the nonlinear energy exchange. $\mathscr{F}$ and $\mathscr{D}$ denote the sources and dissipation of kinetic energy, respectively. Obviously, negative Π_ω leads to an increase of $\overline{KE}_\omega$. At a steady state, the differentiation of equation 3 with respect to ω yields

$$\frac{\partial \Pi_\omega}{\partial \omega} = F(\omega) - D(\omega), \tag{4}$$

where F denotes energy source due to forcing and D denotes energy dissipation. The slope of Π_ω in the frequency domain is positive (negative), when energy source is larger (smaller) than dissipation. Overall,

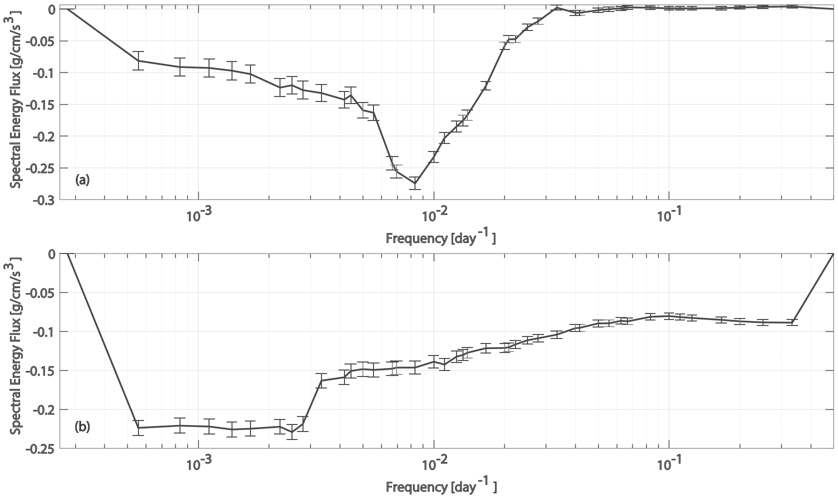

Figure 12. Mean spectral kinetic energy flux Π_ω with respect to ω within Box A (a) and Box B (b). The two boxes are marked in Figure 8b. The variance of Π_ω in each box is represented with the vertical bar at each frequency, as a proxy for the uncertainty of mean Π_ω.

negative Π_ω with a positive slope $\left(\frac{\partial \Pi_\omega}{\partial \omega}\right)$ indicates an accumulation of kinetic energy and an inverse energy cascade from high-frequency to low-frequency components. The regional mean Π_ω with respect to ω in Box A (Figure 8b) is shown in Figure 12a. The variance of Π_ω within Box A is marked with a vertical bar at each frequency (x axis in Figure 12) as a measure of the uncertainty of Π_ω. In Box A, Π_ω reaches its minimum at the frequency of 0.0085 day^{-1} (the period is about 117 days) and the slope of Π_ω is positive within the frequency band of 0.0085–0.033 day^{-1} (the period is 30–117 days), which confirms the inverse energy cascade at subseasonal timescales on the periphery of the ring region. In Box B (Figure 8b), the results are qualitatively the same (Figure 12b). However, the slope of Π_ω is almost flat, which indicates a weak energy accumulation. This is consistent with the model simulations that subseasonal variabilities in Box B are much weaker than those in Box A (Figure 8b).

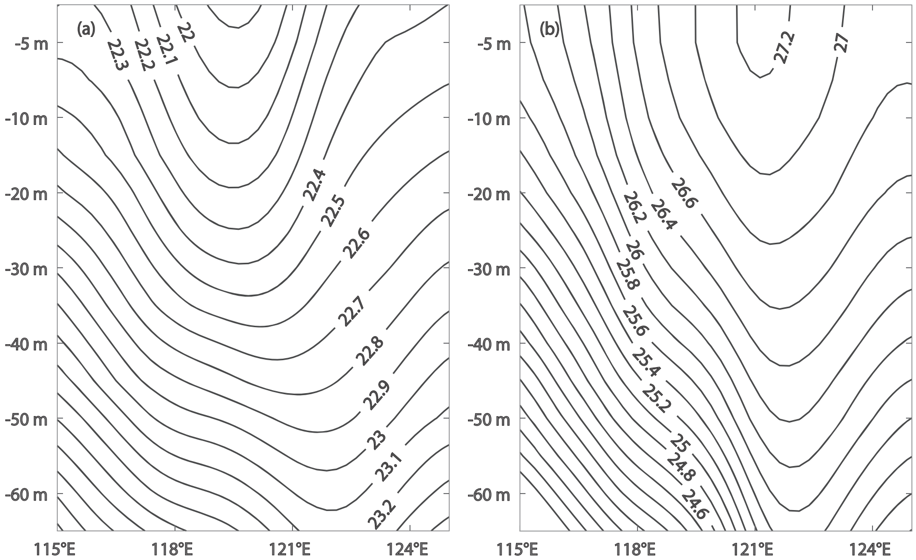

Figure 13. (a) Longitude-depth section of climatological density (a) and temperature (b) along 21°N. Data are obtained from the WOA13. The unit for density is kg m^{-3} and for temperature is °C.

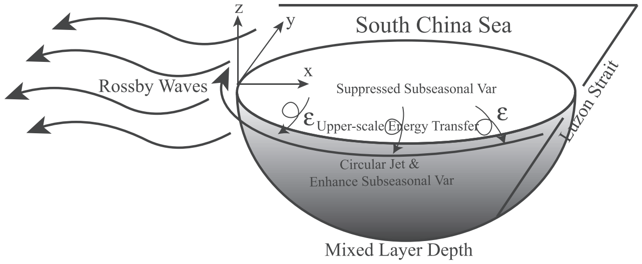

Figure 14. Sketch for the internal variabilities on the subseasonal timescale in the ring region to the west of Luzon Strait.

Consequently, the perturbed kinetic energy can be transferred upscale due to the geostrophic turbulence, and the large-scale circulation is enhanced along the periphery of the ring region (Figure 8b). This also explains the origin of the background currents which transport the kinetic energy and heat around the ring. At the center of the ring region, climatological MLDs are uniformly deep in nature as shown with the longitude-depth sections of density and temperature in Figure 13, using WOA13. The impacts of salinity on density profiles are small. Such deep MLDs in the ring region are reproduced in our simulations, as shown with the white contours in Figure 8b. Considering the simplest form of potential vorticity $PV = \frac{f}{h}$, where f is the Coriolis parameter and h is the MLD, PV tends to be uniform in the center of the ring region adjacent to Luzon Strait. A uniform PV is unfavorable for the generation of perturbed kinetic energy. Therefore, the subseasonal variabilities in the center of the ring region are weak (Figures 5a and 8b). On the contrary, on the edge of the ring region, large PV gradient helps to guide the ocean current along the iso-PV lines along the periphery of the ring region. Due to small L_β which is comparable with the mesoscale in the northern SCS, KE' is converted to and accumulated at large scales, generating a circular mean jet in the azimuthal direction of the ring region which transports T' and KE', as shown in Figures 9 and 10.

4. Conclusions and Discussion

Internal subseasonal variabilities due to nonlinear interactions in SCS are examined using an eddy-resolving model. Oceanic variabilities in SCS are attributable to both external forcing and internal variability. The latter, if large enough relative to the intrinsic timescales of observed variabilities, can play an important role in the responses and feedbacks to all external influences in SCS. It is found that the subseasonal variabilities due to internal variability are enhanced in the northern SCS, and they account for about half of the total observed subseasonal variance. What is of special interest is a ring region to the west of Luzon Strait. The subseasonal SST anomalies are large on the periphery of the ring region, which are even more energetic than those in other regions in the northern SCS. A low-frequency jet is found to be generated around the ring region which has no corresponding forcing in any of the atmospheric fluxes. Thus, it can only stem from the oceanic internal subseasonal variability. Moreover, L_β is comparable to the first baroclinic Rossby radius of deformation L_d. As a result, the kinetic energy is accumulated along the edge of the ring and the mean jet is generated, which is confirmed by examining the spectral kinetic energy flux. In contrast, the center of the ring region is a tranquil blob, where the subseasonal variabilities are much smaller than they are on the periphery. The isopycnal surfaces are largely uniform in the center of the ring region (Figures 8b and 13), which tends to suppress the subseasonal variabilities. On the other hand, the suppressed subseasonal variabilities may also have feedbacks and be favorable for a uniform dynamic environment in the center of the ring region. The dynamics are summarized in the sketch in Figure 14.

The ring patter analyzed in this study is different from the Kuroshio Loop Current, which has been extensively studied (Farris & Wimbush, 1996; Hu et al., 2000; Li et al., 1998; Nan et al., 2015; Z. Zhang et al., 2017). The seasonality of Kuroshio intrusion into SCS can be captured in the control run (not shown). The Kuroshio intrusion is stronger in boreal winter but weaker in boreal summer, since Kuroshio transport is small in winter but large in summer. However, most studies on the Kuroshio Loop Current have focused on seasonal or slower timescales (e.g., al., 2006; Xue et al., 2004; Sun et al., 2016), although the Kuroshio intrusion has subseasonal variabilities on a period of 1–3 months (Jia & Chassignet, 2011; Z. Zhang et al., 2017). The dynamics in the ring region are at subseasonal timescales. The ring region is not discernible from the STDs of total SST or SSH. Moreover, on Day 0 for the ring pattern in the internal run, the high salinity waters above 200 m (which is the typical character of Kuroshio) are clearly present to the east of Luzon Strait. But they are not discernible to the west of Luzon Strait (not shown). Therefore, the water mass in the ring is different from the Kuroshio. In addition, since the ring region is generated due to the internal variability, it is not discernible in the control run (Figure 4b), in which all subseasonal variabilities in external forcing and boundary conditions are maintained.

The ocean-TC interaction is of obvious interest and is the ultimate motivation of this study. Since the TC's impacts on SCS are mainly at the subseasonal timescales, the understanding of the internal subseasonal variability in SCS is necessary for a more complete understanding in the oceanic response to TCs over SCS. As shown in Figure 1, dozens of TCs pass through the northern SCS almost every year. Both the dynamic and thermodynamic environments in the ocean can have significant feedbacks to TCs. Sometimes, the mesoscale structures in the ocean can modify the trajectory and the strength of a TC rapidly, which can greatly reduce the predictability of TCs. Over the ring region to the west of Luzon Strait (the black box in Figure 1), TC occurrence is smaller than the surrounding regions. In addition, the number of eddies in the ring region is also small. For example, using altimeter data, G. Wang et al. (2003) showed that the number of eddies in their Zone Z1 (similar to the ring region) was only half of that in their Zone Z2 which was to the south of Z1. The internal subseasonal variabilities diagnosed in this study indicate that the ring region tends to respond to TCs as a relatively uniform slab. The warm SST anomalies in this region are weak (Figure 8b). As a result, the modifications to TCs are prone to be moderate. Nevertheless, much energy is accumulated on the edge of the ring region, leading to a jet and large SST gradient. Therefore, pronounced warm SST anomalies occur (Figure 8b) and feedbacks to TCs are expected to be strong, which is consistent with the high TC occurrence around the black box in Figure 1.

It is obvious that the internal variability can only be extracted with models, since the impacts from the external forcing can never be fully removed from observations. The merit of a numerical experiment is to unveil a mechanism that can hardly be identified from observations alone. Given that the northern SCS is subject to energetic external forcings with broad spatiotemporal scales, the ring structure at the subseasonal timescales cannot be easily seen in observations (such as Optimum Interpolation Sea Surface Temperature). Therefore, the robustness of current results requires further evaluation with more models and current results are expected to motivate more targeted observations. The inverse cascade found in this study is based on a mesoscale eddy-resolving model. Thus, only the energy transfer from the mesoscale eddy can be captured. More recently, direct cascade from mesoscale to submesoscale and turbulence have been observed (D'Asaro et al., 2011; Z. Zhang, Tian, et al., 2016). Therefore, simulations with a much higher resolution (~1 km) may yield new insights. The entrainment in current simulations seems small. It is mainly attributable to the method for estimating MLD in this study; here MLD is the depth where the temperature is lower than SST by 0.5 °C (Monterey & Levitus, 1997). Thus, the vertical temperature gradient at the bottom of MLD is relatively small, which reduces the estimated entrainment. The thermodynamic equation is established in a σ coordinate (corresponding to equation 1 in z coordinate). The results in z coordinate for the thermodynamic components do not change significantly, and the entrainment remains small (not shown). In addition, the performance of an eddy-resolving model relies on model parameterizations of subgrid processes. For example, the inertial waves are a common consequence of TCs in the ocean. However, so far, the inertial waves and their energy propagation in the ocean have not been routinely parameterized in ocean models (Jochum et al., 2013). Therefore, in order to have a better understanding of the internal subseasonal variability over the SCS, progress in the representation of fine-scale processes and improvement in ocean model parameterization are required in the future.

Appendix A: Derivations of the Heat Budget Equation in the Upper Mixed Layer

The thermodynamic equation for the ocean is (Stevenson & Niiler, 1983)

$$\frac{\partial T}{\partial \mathrm{t}} = -\overrightarrow{V}\cdot\nabla T + \frac{1}{\rho C_p}\frac{\partial Q}{\partial z} + R \tag{A1}$$

where T is the temperature; $\overrightarrow{V} = u\overrightarrow{i} + v\overrightarrow{j} + w\overrightarrow{k}$ is the three-dimensional ocean current vector; u, v, and w are zonal, meridional, and vertical velocities respectively; Q is diabatic heating; C_p is the heat capacity; ρ is the sea water density; and R is a sum of diffusivity and residual. The vertical average within the upper mixed layer is denoted with $\langle\cdot\rangle = \frac{1}{h}\int_{-h}^{0}\cdot\mathrm{d}z$, where h is MLD. Since MLD has significant spatiotemporal variabilities, one can have

$$\frac{\partial\langle T\rangle}{\partial t}=\frac{1}{h}\left(\int_{-h}^{0}\frac{\partial T}{\partial t}dz+\frac{\partial h}{\partial t}T|z=-h\right)-\frac{1}{h}\frac{\partial h}{\partial t}\left(\frac{1}{h}\int_{-h}^{0}T\ \ dz\right)=\left\langle\frac{\partial T}{\partial t}\right\rangle+Ent, \tag{A2}$$

where $Ent=\frac{1}{h}\frac{\partial h}{\partial t}T\big|_{z=-h}-\frac{1}{h}\frac{\partial h}{\partial t}\langle T\rangle$ represent the entrainment. Then, the equation for the mean temperature in the upper mixed layer is

$$\frac{\partial\langle T\rangle}{\partial t}=H_{adv}+V_{adv}+Ent+\frac{Q_{surf}}{\rho C_p h}+\langle R\rangle \tag{A3}$$

where $H_{adv}=-\left\langle\overrightarrow{V}_H\cdot\nabla_{\mathrm{H}}T\right\rangle$, $V_{adv}=-\left\langle w\frac{\partial T}{\partial z}\right\rangle$, and $\overrightarrow{V}_H$ and ∇_H are the horizontal components of $\overrightarrow{V}$ and ∇, respectively.

All variables are decomposed into the background state (denoted with an overbar) and a subseasonal timescale (denoted with a prime); for example, $T=\overline{T}+T'$. For the horizontal advection, one has $H_{adv}=-\left\langle\overline{\overrightarrow{V}}_H\cdot\nabla_{\mathrm{H}}\overline{T}\right\rangle-\left\langle\overline{\overrightarrow{V}}_H\cdot\nabla_{\mathrm{H}}T'\right\rangle-\left\langle\overrightarrow{V}'_H\cdot\nabla_{\mathrm{H}}\overline{T}\right\rangle-\left\langle\overrightarrow{V}'_H\cdot\nabla_{\mathrm{H}}T'\right\rangle$ and $\overline{H}_{adv}=-\left\langle\overline{\overrightarrow{V}}_H\cdot\nabla_{\mathrm{H}}\overline{T}\right\rangle-\overline{\left\langle\overrightarrow{V}'_H\cdot\nabla_{\mathrm{H}}T'\right\rangle}$. Thus, $H'_{adv}=H_{adv}-\overline{H}_{adv}=-\left\langle\overline{\overrightarrow{V}}_H\cdot\nabla_{\mathrm{H}}T'\right\rangle-\left\langle\overrightarrow{V'}_H\cdot\nabla_{\mathrm{H}}\overline{T}\right\rangle-\left(\left\langle\overrightarrow{V}'_H\cdot\nabla_{\mathrm{H}}T'\right\rangle-\overline{\left\langle\overrightarrow{V}'_H\cdot\nabla_{\mathrm{H}}T'\right\rangle}\right)$. Therefore, for the upper mixed layer, the thermodynamic equation on the subseasonal times scale becomes equation 1 in the main text.

Appendix B: Derivations of the Kinetic Energy Equation

The horizontal momentum equations are

$$\left(\frac{\partial}{\partial t}+\overrightarrow{V}\cdot\nabla\right)u-fv=-\frac{\partial\phi}{\partial x}, \tag{B1a}$$

$$\left(\frac{\partial}{\partial t}+\overrightarrow{V}\cdot\nabla\right)v+fu=-\frac{\partial\phi}{\partial y}, \tag{B1b}$$

where f is the Coriolis parameter and ϕ is the geopotential. All other variables have the same meanings as defined in Appendix A. The unresolved and residual terms are omitted. Again, all components are decomposed into the background state (denoted with an overbar) and the subseasonal components (denoted with a prime). One can obtain that

$$\frac{\partial u'}{\partial t}+\left(\overline{\overrightarrow{V}}\cdot\nabla\right)u'+\left(\overrightarrow{V}'\cdot\nabla\right)\overline{u}+\left(\overrightarrow{V}'\cdot\nabla u'-\overline{\overrightarrow{V'}\cdot\nabla u'}\right)-fv'=-\frac{\partial\phi'}{\partial x}, \tag{B2a}$$

$$\frac{\partial v'}{\partial t}+\left(\overline{\overrightarrow{V}}\cdot\nabla\right)v'+\left(\overrightarrow{V}'\cdot\nabla\right)\overline{v}+\left(\overrightarrow{V}'\cdot\nabla v'-\overline{\overrightarrow{V'}\cdot\nabla v'}\right)+fu'=-\frac{\partial\phi'}{\partial y}. \tag{B2b}$$

With the help of continuity equation $\nabla\overrightarrow{V}=0$, $u'\times$ equation B2a + $v'\times$ equation B2b yields

$$\frac{\partial KE'}{\partial t}+\overline{\overrightarrow{V}}\cdot\nabla KE'+\left[u'\left(\overrightarrow{V}'\cdot\nabla\right)\overline{u}+v'\left(\overrightarrow{V}'\cdot\nabla\right)\overline{v}\right]+\left[u'\left(\overrightarrow{V}'\cdot\nabla u'-\overline{\overrightarrow{V'}\cdot\nabla u'}\right)+v'\left(\overrightarrow{V}'\cdot\nabla v'-\overline{\overrightarrow{V'}\cdot\nabla v'}\right)\right]=-\overrightarrow{V}'_H\cdot\nabla_H\phi'. \tag{B3}$$

The vertical momentum equation applying the Boussinesq approximation is

$$\frac{\partial w^{'}}{\partial t} = b^{'}, \tag{B4}$$

where $b^{'} = -g\frac{\rho^{'}}{\overline{\rho}}$ is the buoyance and g is the gravitational acceleration. The sum of $w'\times$ equation B4 and equation B3 yields equation 2 in the main text.

Appendix C: Derivation of the Spectral Energy Equation

The horizontal ocean currents $\vec{u} = (u, v)$ are expressed in Fourier series,

$$\vec{u} = \sum_{\omega} \widehat{\vec{u}_{\omega}} \exp(i\omega t), \tag{C1}$$

where $\widehat{\vec{u}_{\omega}}$ are the amplitudes at frequency ω. The low-frequency and high-frequency variabilities are obtained with low-pass and high-pass filterings

$$\widehat{\overline{\vec{u}}_{\omega}} = \sum_{\omega^{'}<\omega} \widehat{\vec{u}_{\omega^{'}}} \exp\left(i\omega^{'} t\right), \tag{C2a}$$

$$\vec{u}^{'}_{\omega} = \sum_{\omega^{'}>\omega} \widehat{\vec{u}_{\omega^{'}}} \exp\left(i\omega^{'} t\right). \tag{C2b}$$

Note that the overbar here does not denote a temporal mean but a low-frequency component. The horizontal momentum equations with respect to ω are

$$\left(\frac{\partial}{\partial t} + \vec{V}_{\omega}\cdot\nabla\right)u_{\omega} - fv_{\omega} = -\frac{\partial \phi_{\omega}}{\partial x}, \tag{C3a}$$

$$\left(\frac{\partial}{\partial t} + \vec{V}_{\omega}\cdot\nabla\right)v_{\omega} + fu_{\omega} = -\frac{\partial \phi_{\omega}}{\partial y}, \tag{C3b}$$

with the help of equations C2a and C2b; all components are decomposed into the low-frequency and high-frequency components. Thus, the kinetic energy equation at high-frequency can be written as

$$\frac{\partial KE^{'}_{\omega}}{\partial t} + \overline{\vec{V}}_{\omega}\cdot\nabla KE^{'}_{\omega} + \vec{u}^{'}_{\omega}\cdot\left[\left(\vec{u}^{'}_{\omega}\cdot\nabla\right)\overline{\vec{u}}_{\omega}\right] + \left[u^{'}_{\omega}\left(\vec{V}^{'}_{\omega}\cdot\nabla u^{'}_{\omega} - \overline{\vec{V}^{'}_{\omega}\cdot\nabla u^{'}_{\omega}}\right) + v^{'}_{\omega}\left(\vec{V}^{'}_{\omega}\cdot\nabla v^{'}_{\omega} - \overline{\vec{V}^{'}_{\omega}\cdot\nabla v^{'}_{\omega}}\right)\right] = -\vec{V}^{'}_{H}\omega\cdot\nabla_{H}\phi^{'}_{\omega}. \tag{C4}$$

where $KE^{'}_{\omega} = \frac{1}{2}\vec{u}^{'}_{\omega}\cdot\vec{u}^{'}_{\omega}$ denotes the high-frequency kinetic energy at any ω. $-\vec{u}^{'}_{\omega}\cdot\left[\left(\vec{u}^{'}_{\omega}\cdot\nabla\right)\overline{\vec{u}}_{\omega}\right]$ stands for the kinetic energy exchange between the high-frequency and low-frequency scales.

Following Scott and Wang (2005), the kinetic energy equation for the low-frequency kinetic energy can be written as

$$\frac{\partial \overline{KE}_{\omega}}{\partial t} = -\Pi_{\omega} + \mathscr{F} - \mathscr{D}, \tag{C5}$$

where $\overline{KE}_{\omega} = \frac{1}{2}\overline{\vec{u}}_{\omega}\cdot\overline{\vec{u}}_{\omega}$ denotes the low-frequency kinetic energy at a given frequency ω. $\Pi_{\omega} = -\vec{u}^{'}_{\omega}\cdot\left[\left(\vec{u}^{'}_{\omega}\cdot\nabla\right)\overline{\vec{u}}_{\omega}\right]$ denotes the nonlinear energy exchange.

Acknowledgments

This work is supported by grants from the National Key Project of Research and Development Plan of China (2016YFC1401905), the National Programme on Global Change and Air-Sea Interaction (GASI-IPOVAI-04, GASI-IPOVAI-01-02, and GASI-IPOVAI-02), the National Natural Science Foundation of China (41621064, 41690121, and 41690120), and the China Ocean Mineral Resources Research and Development Association Program (DY135-E2-3-01 and DY135-E2-3-05). RM is grateful for the Visiting Faculty at the Indian Institute of Technology - Bombay, India.The reanalysis and data products for this paper are properly cited and referred to in the reference list. The other data and model output are available online (https://zenodo.org/record/3529583#.XcOBUoWf6kz).

References

Cai, S., Long, X., Wu, R., & Wang, S. (2008). Geographical and monthly variability of the first baroclinic Rossby radius of deformation in the South China Sea. *Journal of Marine Systems*, *74*(1-2), 711–720. https://doi.org/10.1016/j.jmarsys.2007.12.008

Carton, J. A., Chepurin, G., & Cao, X. (2000). A simple ocean data assimilation analysis of the global upper ocean 1950–95. Part II: Results. *Journal of Physical Oceanography*, *30*(2), 311–326. https://doi.org/10.1175/1520-0485(2000)030<0311:ASODAA>2.0.CO;2

Carton, J. A., Chepurin, G., Cao, X. H., & Giese, B. (2000). A simple ocean data assimilation analysis of the global upper ocean 1950-95. Part I: Methodology. *Journal of Physical Oceanography*, *30*(2), 294–309. https://doi.org/10.1175/1520-0485(2000)030<0294:ASODAA>2.0.CO;2

Carton, J. A., & Giese, B. S. (2008). A reanalysis of ocean climate using Simple Ocean Data Assimilation (SODA). *Monthly Weather Review*, *136*(8), 2999–3017. https://doi.org/10.1175/2007MWR1978.1

Caruso, M. J., Gawarkiewicz, G. G., & Beardsley, R. C. (2006). Interannual variability of the Kuroshio intrusion in the South China Sea. *Journal of Oceanography*, *62*(4), 559–575. https://doi.org/10.1007/s10872-006-0076-0

Centurioni, L. R., Niiler, P. P., & Lee, D.-K. (2004). Observations of inflow of Philippine Sea surface water into the South China Sea through the Luzon Strait. *Journal of Physical Oceanography*, *34*(1), 113–121. https://doi.org/10.1175/1520-0485(2004)034<0113:OOIOPS>2.0.CO;2

Chelton, D. B., de Szoeke, R. A., Schlax, M. G., Naggar, K. E., & Siwertz, N. (1998). Geographical variability of the first baroclinic Rossby radius of deformation. *Journal of Physical Oceanography*, *28*(3), 433–460. https://doi.org/10.1175/1520-0485(1998)028<0433:GVOTFB>2.0.CO;2

Chelton, D. B., & Schlax, M. G. (1996). Global observations of oceanic Rossby waves. *Science*, *272*(5259), 234–238. https://doi.org/10.1126/science.272.5259.234

Chen, G., Xue, H., Wang, D., & Xie, Q. (2013). Observed near-inertial kinetic energy in the northwestern South China Sea. *Journal of Geophysical Research: Oceans*, *118*, 4965–4977. https://doi.org/10.1002/jgrc.20371

Chiang, T. L., Wu, C. R., & Oey, L. Y. (2011). Typhoon Kai-Tak: An ocean's perfect storm. *Journal of Physical Oceanography*, *41*(1), 221–233. https://doi.org/10.1175/2010JPO4518.1

Dare, R. A., & McBride, J. L. (2011). Sea surface temperature response to tropical cyclones. *Monthly Weather Review*, *139*(12), 3798–3808. https://doi.org/10.1175/MWR-D-10-05019.1

D'Asaro, E., Lee, C., Rainville, L., Harcourt, R., & Thomas, L. (2011). Enhanced turbulence and energy dissipation at ocean fronts. *Science*, *332*(6027), 318–322. https://doi.org/10.1126/science.1201515

Ding, Y., Li, C., & Liu, Y. (2004). Overview of the South China sea monsoon experiment. *Advances in Atmospheric Sciences*, *21*, 343–360. https://doi.org/10.1007/BF02915563

Ducet, N., Le Traon, P. Y., & Reverdin, G. (2000). Global high-resolution mapping of ocean circulation from TOPEX/Poseidon and ERS-1 and -2. *Journal of Geophysical Research*, *105*(C8), 19,477–19,498. https://doi.org/10.1029/2000JC900063

Emanuel, K. (2001). Contribution of tropical cyclones to meridional heat transport by the oceans. *Journal of Geophysical Research*, *106*(D14), 14,771–14,781. https://doi.org/10.1029/2000JD900641

Farris, A., & Wimbush, M. (1996). Wind-induced Kuroshio intrusion into the South China Sea. *Journal of Oceanography*, *52*(6), 771–784. https://doi.org/10.1007/BF02239465

Gordon, A. L., Huber, B. A., Metzger, E. J., Susanto, R. D., Hurlburt, H. E., & Adi, T. R. (2012). South China Sea throughflow impact on the Indonesian throughflow. *Geophysical Research Letters*, *39*, L11602. https://doi.org/10.1029/2012GL052021

Gordon, A. L., Susanto, R. D., & Vranes, K. (2003). Cool Indonesian throughflow as a consequence of restricted surface layer flow. *Nature*, *425*(6960), 824–828. https://doi.org/10.1038/nature02038

Graham, N. E., & Barnett, T. P. (1987). Sea surface temperature, surface wind divergence, and convection over tropical oceans. *Science*, *238*(4827), 657–659. https://doi.org/10.1126/science.238.4827.657

Guan, S., Zhao, W., Huthnance, J., Tian, J., & Wang, J. (2014). Observed upper ocean response to typhoon Megi (2010) in the Northern South China Sea. *Journal of Geophysical Research: Oceans*, *119*, 3134–3157. https://doi.org/10.1002/2013JC009661

Hart, R. E. (2011). An inverse relationship between aggregate northern hemisphere tropical cyclone activity and subsequent winter climate. *Geophysical Research Letters*, *38*, L01705. https://doi.org/10.1029/2010GL045612

Holton, J. R., & Hakim, G. J. (2013). Chapter 10—The general circulation. In *An introduction to dynamic meteorology* (Fifth ed., pp. 325–375). Amsterdam: Academic Press.

Hu, J., Kawamura, H., Hong, H., & Qi, Y. (2000). A review on the currents in the South China Sea: Seasonal circulation, South China Sea warm current and Kuroshio Intrusion. *Journal of Oceanography*, *56*(6), 607–624. https://doi.org/10.1023/A:1011117531252

Hu, J., Zheng, Q., Sun, Z., & Tai, C.-K. (2012). Penetration of nonlinear Rossby eddies into South China Sea evidenced by cruise data. *Journal of Geophysical Research*, *117*, C03010. https://doi.org/10.1029/2011JC007525

Jansen, M. F., Ferrari, R., & Mooring, T. A. (2010). Seasonal versus permanent thermocline warming by tropical cyclones. *Geophysical Research Letters*, *37*, L03602. https://doi.org/10.1029/2009GL041808

Jia, Y., & Chassignet, E. P. (2011). Seasonal variation of eddy shedding from the Kuroshio intrusion in the Luson Strait. *Journal of Oceanography*, *67*(5), 601–611. https://doi.org/10.1007/s10872-011-0060-1

Jochum, M., Briegleb, B. P., Danabasoglu, G., Large, W. G., Norton, N. J., Jayne, S. R., et al. (2013). The impact of oceanic near-inertial waves on climate. *Journal of Climate*, *26*(9), 2833–2844. https://doi.org/10.1175/JCLI-D-12-00181.1

Jochum, M., & Murtugudde, R. (2004). Internal variability of the tropical Pacific Ocean. *Geophysical Research Letters*, *31*, L14309. https://doi.org/10.1029/2004GL020488

Jochum, M., & Murtugudde, R. (2005). Internal variability of Indian Ocean SST. *Journal of Climate*, *18*(18), 3726–3738. https://doi.org/10.1175/JCLI3488.1

Jochum, M., & Murtugudde, R. (2006). Temperature advection by tropical instability waves. *Journal of Physical Oceanography*, *36*, 592–605. https://doi.org/10.1175/JPO2870.1

Jochum, M., Murtugudde, R., Malanotte-Rizzoli, P., & Busalacchi, A. J. (2004). Internal variability of the tropical Atlantic Ocean. In *Earth's climate: The ocean–atmosphere interaction*, *Geophysical Monographs Series* (Vol. 147, pp. 181–187). Washington, DC: American Geophysical Union.

Lau, K. M., Ding, Y., Wang, J.-T., Johnson, R., Keenan, T., Cifelli, R., et al. (2000). A report of the field operations and early results of the South China Sea Monsoon Experiment (SCSMEX). *Bulletin of the American Meteorological Society*, *81*(6), 1261–1270. https://doi.org/10.1175/1520-0477(2000)081<1261:AROTFO>2.3.CO;2

Li, L., Nowlin, W. D. Jr., & Jilan, S. (1998). Anticyclonic rings from the Kuroshio in the South China Sea. *Deep Sea Research Part I: Oceanographic Research Papers*, *45*(9), 1469–1482. https://doi.org/10.1016/S0967-0637(98)00026-0

Lin, I. I., Chen, C.-H., Pun, I.-F., Liu, W. T., & Wu, C.-C. (2009). Warm ocean anomaly, air sea fluxes, and the rapid intensification of tropical cyclone Nargis (2008). *Geophysical Research Letters*, *36*, L03817. https://doi.org/10.1029/2008GL035815

Lin, I. I., Wu, C.-C., Emanuel, K. A., Lee, I. H., Wu, C.-R., & Pun, I.-F. (2005). The interaction of Supertyphoon Maemi (2003) with a warm ocean eddy. *Monthly Weather Review*, *133*(9), 2635–2649. https://doi.org/10.1175/MWR3005.1

Lin, I. I., Wu, C.-C., Pun, I.-F., & Ko, D.-S. (2008). Upper-ocean thermal structure and the Western North Pacific category 5 typhoons. Part I: Ocean features and the category 5 typhoons' intensification. *Monthly Weather Review*, *136*(9), 3288–3306. https://doi.org/10.1175/2008MWR2277.1

Lin, Y.-C., Oey, L.-Y., Wang, J., & Liu, K.-K. (2016). Rossby waves and eddies observed at a temperature mooring in Northern South China Sea. *Journal of Physical Oceanography*, *46*(2), 517–535. https://doi.org/10.1175/JPO-D-15-0094.1

Liu, Z., Yang, H., & Liu, Q. (2001). Regional dynamics of seasonal variability in the South China Sea. *Journal of Physical Oceanography*, *31*(1), 272–284. https://doi.org/10.1175/1520-0485(2001)031<0272:RDOSVI>2.0.CO;2

Locarnini, R. A., Mishonov, A. V., Antonov, J. I., Boyer, T. P., Garcia, H. E., Baranova, O. K., et al. (2013). In S. Levitus & A. Mishonov (Eds.), Technical*World ocean atlas 2013, volume 1: Temperature*, NOAA Atlas NESDIS (Vol. *73*, p. 40). Washington, DC: U.S. Government Printing Office.

Lu, J., & Liu, Q. (2013). Gap-leaping Kuroshio and blocking westward-propagating Rossby wave and eddy in the Luzon Strait. *Journal of Geophysical Research: Oceans*, *118*, 1170–1181. https://doi.org/10.1002/jgrc.20116

Metzger, E. J., & Hurlburt, H. E. (1996). Coupled dynamics of the South China Sea, the Sulu Sea, and the Pacific Ocean. *Journal of Geophysical Research*, *101*(C5), 12,331–12,352. https://doi.org/10.1029/95JC03861

Monterey, G. I., & Levitus, S. (1997). Seasonal variability of mixed layer depth for the world ocean. US Department of Commerce, National Oceanic and Atmospheric Administration, National Environmental Satellite, Data, and Information Service.

Nan, F., Xue, H., & Yu, F. (2015). Kuroshio intrusion into the South China Sea: A review. *Progress in Oceanography*, *137*, 314–333. https://doi.org/10.1016/j.pocean.2014.05.012

Price, J. F., Morzel, J., & Niiler, P. P. (2008). Warming of SST in the cool wake of a moving hurricane. *Journal of Geophysical Research*, *113*, C07010. https://doi.org/10.1029/2007JC004393

Qu, T., Mitsudera, H., & Yamagata, T. (2000). Intrusion of the North Pacific waters into the South China Sea. *Journal of Geophysical Research*, *105*(C3), 6415–6424. https://doi.org/10.1029/1999JC900323

Qu, T., Song, Y. T., & Yamagata, T. (2009). An introduction to the South China Sea throughflow: Its dynamics, variability, and application for climate. *Dynamics of Atmospheres and Oceans*, *47*(1-3), 3–14. https://doi.org/10.1016/j.dynatmoce.2008.05.001

Qu, T. D., Du, Y., & Sasaki, H. (2006). South China Sea throughflow: A heat and freshwater conveyor. *Geophysical Research Letters*, *33*, L23617. https://doi.org/10.1029/2006GL028350

Reynolds, R. W., Rayner, N. A., Smith, T. M., Stokes, D. C., & Wang, W. (2002). An improved in situ and satellite SST analysis for climate. *Journal of Climate*, *15*(13), 1609–1625. https://doi.org/10.1175/1520-0442(2002)015<1609:AIISAS>2.0.CO;2

Saha, S., Moorthi, S., Pan, H.-L., Wu, X., Wang, J., Nadiga, S., et al. (2010). The NCEP climate forecast system reanalysis. *Bulletin of the American Meteorological Society*, *91*(8), 1015–1058. https://doi.org/10.1175/2010BAMS3001.1

Schade, L. R., & Emanuel, K. A. (1999). The ocean's effect on the intensity of tropical cyclones: Results from a simple coupled atmosphere–ocean model. *Journal of the Atmospheric Sciences*, *56*(4), 642–651. https://doi.org/10.1175/1520-0469(1999)056<0642:TOSEOT>2.0.CO;2

Schott, F. A., Xie, S.-P., & McCreary, J. P. (2009). Indian Ocean circulation and climate variability. *Reviews of Geophysics*, *47*, RG1002. https://doi.org/10.1029/2007RG000245

Scott, R. B., & Arbic, B. K. (2007). Spectral energy fluxes in geostrophic turbulence: Implications for ocean energetics. *Journal of Physical Oceanography*, *37*(3), 673–688. https://doi.org/10.1175/JPO3027.1

Scott, R. B., & Wang, F. (2005). Direct evidence of an oceanic inverse kinetic energy cascade from satellite altimetry. *Journal of Physical Oceanography*, *35*(9), 1650–1666. https://doi.org/10.1175/JPO2771.1

Sengupta, D., Goswami, B. N., & Senan, R. (2001). Coherent intraseasonal oscillations of ocean and atmosphere during the Asian Summer Monsoon. *Geophysical Research Letters*, *28*(21), 4127–4130. https://doi.org/10.1029/2001GL013587

Shchepetkin, A. F., & McWilliams, J. C. (2003). A method for computing horizontal pressure-gradient force in an oceanic model with a nonaligned vertical coordinate. *Journal of Geophysical Research*, *108*(C3), 3090. https://doi.org/10.1029/2001JC001047

Shchepetkin, A. F., & McWilliams, J. C. (2005). The regional oceanic modeling system (ROMS): A split-explicit, free-surface, topography-following-coordinate oceanic model. *Ocean Modelling*, *9*(4), 347–404. https://doi.org/10.1016/j.ocemod.2004.08.002

Shchepetkin, A. F., & McWilliams, J. C. (2011). Accurate Boussinesq oceanic modeling with a practical, "stiffened" equation of state. *Ocean Modelling*, *38*(1-2), 41–70. https://doi.org/10.1016/j.ocemod.2011.01.010

Sheu, W.-J., Wu, C.-R., & Oey, L.-Y. (2010). Blocking and westward passage of eddies in the Luzon Strait. *Deep Sea Research Part II: Topical Studies in Oceanography*, *57*(19-20), 1783–1791. https://doi.org/10.1016/j.dsr2.2010.04.004

Shinoda, T., Hendon, H. H., & Glick, J. (1998). Intraseasonal variability of surface fluxes and sea surface temperature in the tropical western Pacific and Indian Oceans. *Journal of Climate*, *11*(7), 1685–1702. https://doi.org/10.1175/1520-0442(1998)011<1685:IVOSFA>2.0.CO;2

Shu, Y., Zhu, J., Wang, D., Yan, C., & Xiao, X. (2009). Performance of four sea surface temperature assimilation schemes in the South China Sea. *Continental Shelf Research*, *29*(11-12), 1489–1501. https://doi.org/10.1016/j.csr.2009.03.016

Sriver, R. L., & Huber, M. (2007). Observational evidence for an ocean heat pump induced by tropical cyclones. *Nature*, *447*(7144), 577–580. https://doi.org/10.1038/nature05785

Stevenson, J. W., & Niiler, P. P. (1983). Upper ocean heat budget during the Hawaii-to-Tahiti Shuttle Experiment. *Journal of Physical Oceanography*, *13*(10), 1894–1907. https://doi.org/10.1175/1520-0485(1983)013<1894:UOHBDT>2.0.CO;2

Sun, J., Oey, L., Xu, F., & Lin, Y.-C. (2017). Sea level rise, surface warming, and the weakened buffering ability of South China Sea to strong typhoons in recent decades. *Scientific Reports*, *7*(1), 7418. https://doi.org/10.1038/s41598-017-07572-3

Sun, J., & Oey, L.-Y. (2015). The influence of ocean on Typhoon Nuri (2008). *Monthly Weather Review*, *143*(11), 4493–4513. https://doi.org/10.1175/MWR-D-15-0029.1

Sun, J., Oey, L.-Y., Chang, R., Xu, F., & Huang, S.-M. (2015). Ocean response to Typhoon Nuri (2008) in western North Pacific and South China Sea. *Ocean Dynamics*, *65*(5), 735–749. https://doi.org/10.1007/s10236-015-0823-0

Sun, Z., Zhang, Z., Zhao, W., & Tian, J. (2016). Interannual modulation of eddy kinetic energy in the northeastern South China Sea as revealed by an eddy-resolving OGCM. *Journal of Geophysical Research: Oceans*, *121*, 3190–3201. https://doi.org/10.1002/2015JC011497

Teague, W. J., Jarosz, E., Wang, D. W., & Mitchell, D. A. (2007). Observed oceanic response over the upper continental slope and outer shelf during hurricane Ivan. *Journal of Physical Oceanography*, *37*(9), 2181–2206. https://doi.org/10.1175/JPO3115.1

Tian, J., Yang, Q., Liang, X., Xie, L., Hu, D., Wang, F., & Qu, T. (2006). Observation of Luzon Strait transport. *Geophysical Research Letters*, *33*, L19607. https://doi.org/10.1029/2006GL026272

Tseng, Y.-H., Jan, S., Dietrich, D. E., Lin, I.-I., Chang, Y.-T., & Tang, T.-Y. (2010). Modeled oceanic response and sea surface cooling to Typhoon Kai-Tak. *Terrestrial, Atmospheric and Oceanic Sciences*, *21*, 85–98. https://doi.org/10.3319/TAO.2009.06.08.02(IWNOP)

Umlauf, L., & Burchard, H. (2003). A generic length-scale equation for geophysical turbulence models. *Journal of Marine Research*, *61*(2), 235–265. https://doi.org/10.1357/002224003322005087

Vallis, G. K. (2006). *Atmospheric and oceanic fluid dynamics* (Vol. 745). Cambridge: Cambridge University Press.

Waliser, D. E., Murtugudde, R., & Lucas, L. E. (2003). Indo-Pacific Ocean response to atmospheric intraseasonal variability: 1. Austral summer and the Madden-Julian Oscillation. *Journal of Geophysical Research*, *108*(C5), 3160. https://doi.org/10.1029/2002JC001620

Waliser, D. E., Murtugudde, R., & Lucas, L. E. (2004). Indo-Pacific Ocean response to atmospheric intraseasonal variability: 2. Boreal summer and the intraseasonal oscillation. *Journal of Geophysical Research*, *109*, C03030. https://doi.org/10.1029/2003JC002002

Wang, B., Huang, F., Wu, Z., Yang, J., Fu, X., & Kikuchi, K. (2009). Multi-scale climate variability of the South China Sea monsoon: A review. *Dynamics of Atmospheres and Oceans*, *47*(1-3), 15–37. https://doi.org/10.1016/j.dynatmoce.2008.09.004

Wang, B., LinHo, Y. Z., & Lu, M.-M. (2004). Definition of South China Sea monsoon onset and commencement of the East Asia summer monsoon. *Journal of Climate*, *17*(4), 699–710. https://doi.org/10.1175/2932.1

Wang, C., Wang, W., Wang, D., & Wang, Q. (2006). Interannual variability of the South China Sea associated with El Niño. *Journal of Geophysical Research*, *111*, C03023. https://doi.org/10.1029/2005JC003333

Wang, G., Su, J., & Chu, P. C. (2003). Mesoscale eddies in the South China Sea observed with altimeter data. *Geophysical Research Letters*, *30*(21), 2121. https://doi.org/10.1029/2003GL018532

Warner, J. C., Sherwood, C. R., Arango, H. G., & Signell, R. P. (2005). Performance of four turbulence closure models implemented using a generic length scale method. *Ocean Modelling*, *8*(1-2), 81–113. https://doi.org/10.1016/j.ocemod.2003.12.003

Wu, C.-C., Lee, C.-Y., & Lin, I. I. (2007). The effect of the ocean eddy on tropical cyclone intensity. *Journal of the Atmospheric Sciences*, *64*(10), 3562–3578. https://doi.org/10.1175/JAS4051.1

Wu, C.-R., & Chiang, T.-L. (2007). Mesoscale eddies in the northern South China Sea. *Deep Sea Research Part II: Topical Studies in Oceanography*, *54*(14-15), 1575–1588. https://doi.org/10.1016/j.dsr2.2007.05.008

Xie, S.-P., Chang, C.-H., Xie, Q., & Wang, D. (2007). Intraseasonal variability in the summer South China Sea: Wind jet, cold filament, and recirculations. *Journal of Geophysical Research*, *112*, C10008. https://doi.org/10.1029/2007JC004238

Xiu, P., Chai, F., Shi, L., Xue, H., & Chao, Y. (2010). A census of eddy activities in the South China Sea during 1993–2007. *Journal of Geophysical Research*, *115*, C03012. https://doi.org/10.1029/2009JC005657

Xu, F.-H., & Oey, L.-Y. (2015). Seasonal SSH variability of the northern South China Sea. *Journal of Physical Oceanography*, *45*(6), 1595–1609. https://doi.org/10.1175/JPO-D-14-0193.1

Xue, H., Chai, F., Pettigrew, N., Xu, D., Shi, M., & Xu, J. (2004). Kuroshio intrusion and the circulation in the South China Sea. *Journal of Geophysical Research*, *109*, C02017. https://doi.org/10.1029/2002JC001724

Yang, H., & Liu, Q. (2003). Forced Rossby wave in the northern South China Sea. *Deep Sea Research Part I: Oceanographic Research Papers*, *50*(7), 917–926. https://doi.org/10.1016/S0967-0637(03)00074-8

Yang, H., Wu, L., Liu, H., & Yu, Y. (2013). Eddy energy sources and sinks in the South China Sea. *Journal of Geophysical Research: Oceans*, *118*, 4716–4726. https://doi.org/10.1002/jgrc.20343

Yang, L., Zhou, L., Li, S., & Wei, Z. (2018). Spreading of the South Pacific tropical water and Antarctic intermediate water over the maritime continent. *Journal of Geophysical Research: Oceans*, *123*, 4423–4446. https://doi.org/10.1029/2018JC013831

Ying, M., Zhang, W., Yu, H., Lu, X., Feng, J., Fan, Y., et al. (2014). An overview of the China Meteorological Administration tropical cyclone database. *Journal of Atmospheric and Oceanic Technology*, *31*(2), 287–301. https://doi.org/10.1175/JTECH-D-12-00119.1

Yuan, D., Han, W., & Hu, D. (2006). Surface Kuroshio path in the Luzon Strait area derived from satellite remote sensing data. *Journal of Geophysical Research*, *111*, C11007. https://doi.org/10.1029/2005JC003412

Zhang, H., Chen, D., Zhou, L., Liu, X., Ding, T., & Zhou, B. (2016). Upper ocean response to typhoon Kalmaegi (2014). *Journal of Geophysical Research: Oceans*, *121*, 6520–6535. https://doi.org/10.1002/2016JC012064

Zhang, L., Wang, B., & Zeng, Q. (2009). Impact of the Madden–Julian Oscillation on summer rainfall in Southeast China. *Journal of Climate*, *22*(2), 201–216. https://doi.org/10.1175/2008JCLI1959.1

Zhang, M., Zhou, L., Fu, H., Jiang, L., & Zhang, X. (2016). Assessment of intraseasonal variabilities in China Ocean reanalysis (CORA). *Acta Oceanologica Sinica*, *35*(3), 90–101. https://doi.org/10.1007/s13131-016-0820-2

Zhang, Z., Tian, J., Qiu, B., Zhao, W., Chang, P., Wu, D., & Wan, X. (2016). Observed 3D structure, generation, and dissipation of oceanic mesoscale eddies in the South China Sea. *Scientific Reports*, *6*, 24349. https://doi.org/10.1038/srep24349

Zhang, Z., Zhao, W., Qiu, B., & Tian, J. (2017). Anticyclonic eddy sheddings from Kuroshio loop and the accompanying cyclonic eddy in the northeastern South China Sea. *Journal of Physical Oceanography*, *47*, 1243–1259. https://doi.org/10.1175/JPO-D-16-0185.1

Zheng, Q., Tai, C.-K., Hu, J., Lin, H., Zhang, R.-H., Su, F.-C., & Yang, X. (2011). Satellite altimeter observations of nonlinear Rossby eddy-Kuroshio interaction at the Luzon Strait. *Journal of Oceanography*, *67*(4), 365–376. https://doi.org/10.1007/s10872-011-0035-2

Zheng, Z. W., Ho, C. R., & Kuo, N. J. (2008). Importance of pre-existing oceanic conditions to upper ocean response induced by Super Typhoon Hai-Tang. *Geophysical Research Letters*, *35*, L20603. https://doi.org/10.1029/2008GL035524

Zheng, Z. W., Ho, C. R., Zheng, Q., Lo, Y. T., Kuo, N. J., & Gopalakrishnan, G. (2010). Effects of preexisting cyclonic eddies on upper ocean responses to category 5 typhoons in the western North Pacific. *Journal of Geophysical Research*, *115*, C09013. https://doi.org/10.1029/2009JC005562

Zhou, L., Chen, D., Karnauskas, K. B., Wang, C., Lei, X., Wang, W., et al. (2018). Introduction to special section on oceanic responses and feedbacks to tropical cyclones. *Journal of Geophysical Research: Oceans*, *123*, 742–745. https://doi.org/10.1002/2018JC013809

Zhou, L., Murtugudde, R., & Jochum, M. (2008). Seasonal influence of Indonesian Throughflow in the southwestern Indian Ocean. *Journal of Physical Oceanography*, *38*(7), 1529–1541. https://doi.org/10.1175/2007JPO3851.1

Zhou, L., Sobel, A. H., & Murtugudde, R. (2012). Kinetic energy budget for the Madden–Julian Oscillation in a multiscale framework. *Journal of Climate*, *25*(15), 5386–5403. https://doi.org/10.1175/JCLI-D-11-00339.1

Zhou, W., & Chan, J. C. L. (2007). ENSO and the South China Sea summer monsoon onset. *International Journal of Climatology*, *27*(2), 157–167. https://doi.org/10.1002/joc.1380

Zhuang, W., Xie, S. P., Wang, D., Taguchi, B., Aiki, H., & Sasaki, H. (2010). Intraseasonal variability in sea surface height over the South China Sea. *Journal of Geophysical Research*, *115*, C04010. https://doi.org/10.1029/2009JC005647